Iraqi Geological Journal

Journal homepage: https://www.igj-iraq.org

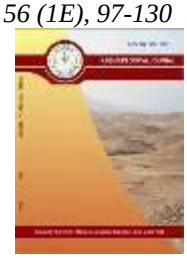

Detecting Oxides Mineralization Utilizing Remote Sensing and Comprehensive Mineralogical Analysis: A Case Study Around Mikbi-Zayatit District, South Eastern Desert, Egypt

Hatem El-Desoky[1], Ali Shebl[2,3], Hamada El-Awny[1], Mahmoud El-Rahmany[1], Omar Soliman[4]

[1] Geology Department, Faculty of Science, Al-Azhar University, Cairo, Egypt.
[2] Department of Mineralogy and Geology, University of Debrecen, Debrecen, Hungary.
[3] Department of Geology, Tanta University, Tanta, Egypt
[4] Raw material engineer, Emirates steel, UAE.

Received:
20 October 2022

Accepted:
16 January 2023

Published:
31 May 2023

Abstract

Undoubtedly, involving more tools, datasets, and techniques for detecting the mineralized areas sharply narrow the zones to be investigated and delivered, in most cases highly potential zones. Consequently, this study is an attempt to apply remote sensing data including Sentinel 2 and ASTER, field observations, petrography of the hydrothermal alteration processes, ore microscopic investigations, X-ray examinations, and EDX analysis to detect and emphasize mineralization types at Wadi Mikbi and Wadi Zayatit district, South Eastern Desert, Egypt. Towards accurate lithological mapping, remote sensing data, previous geological maps, and the field investigations recorded serpentinites, ophiolitic metagabbros, amphibolites, epidosite, arc-related metasediments (schists and quartzites), metagabbro-tonalite complex, dunite, olivine gabbros, and granitic rocks encountered in the study district. Additionally, various hydrothermal alteration zones have been primarily outlined using ASTER and Sentinel 2 data by implementing informative band ratios and constrained energy minimization techniques. The mineralogical studies have confirmed most of the remotely-detected hydrothermal alteration minerals. Ore microscopy, XRD technique, and EDX microchemical analysis of representative mineralized samples of the study district identified magnetite, ilmenite, titanomagnetite, chromite, magnesioferrite, quartz, apatite, clinochlore, plagioclase, pyroxene and epidote. Cross-linking remote sensing results, field observations and laboratory studies revealed that the dominant hydrothermal alteration processes include oxidization, serpentinization, carbonatization, epidotization, silicification, zoisitization, muscovitization, sericitization, and chloritization. Spatial overlay analysis of the resultant altered features, structural dissection, field observations, and analytical studies were integrated to build a mineral potentiality map of the study district.

Keywords: Remote sensing; Alteration zones; Ore mineralogy; Eastern Desert; Egypt

1. Introduction

Meticulous investigating of Neoproterozoic basement rocks (with their various assemblages including the ophiolitic and non-ophiolitic complexes) is still considered one of the most important factors for resolving the origin of tectonically-complicated terranes, deciphering geodynamic settings, and crust-mantle interaction processes (Abd El-Wahed et al., 2019), and pointing various economic

DOI: 10.46717/igj.56.1E.8ms-2023-5-18

mineral deposits (Shebl et al., 2021a), especially in the Egyptian Eastern Desert. The latter has been tectonically-divided into Northern Eastern Desert (NED) which is mainly considered an extensional province, Central Eastern Desert (CED), where the metamorphic domes are mostly evident and are considered a wrench province, and Southern Eastern Desert (SED), where the compressional regime is dominated (Hamimi et al., 2022). Tectonic regimes result in different lithological assemblages in NED, CED, and SED **(**Hamimi et al., 2022). The current study district (Wadi Mikbi and Wadi Zayatit district, South Eastern Desert, Egypt) is a part of SED. The SED Neoproterozoic basement rocks have been previously studied by several authors (Basta, and Takla, 1968; Basta and Kamel, 1970; Kotb et al., 1980; EGSMA, 1988; Abu El-Russ, 1991; Madbouly, 2000; Abd El-Wahab, 2011; Maurice et al., 2013; Ramadan et al., 2016; Salem, 2017 & 2018; Soliman et al., 2021; Abdel-Rahman et al., 2022; El-Desoky et al., 2022a and El-Desoky et al., 2022b) and reporting that SED ophiolitic assemblages include mantle and basal crustal sections of the Neoproterozoic sequences formed in the Arabian Nubian Shield (ANS) along the major suture zones (Shackleton et al., 1980; Ries et al., 1983; Stern, 1994; Loizenbauer et al., 2001; Stern et al., 2004; Ali et al., 2010; Abdel-Karim et al., 2016 and El-Bahariya, 2019 & 2021).

The recent gold exploitation within SED has already proved their promising gold content. Thus, the current research (for the first time over the study district) integrated remote sensing data including Sentinel 2 and ASTER with field observations, petrographic investigations of hydrothermal alteration types, ore microscopic examinations, X-ray measurements, and EDX microchemical analysis to outline the potential mineralization zones accurately. The utilized remote sensing data provide a quick, acceptable, and efficient tool for delineating the alteration zones {Formatting Citation} and discriminating the exposed rock units (Hamimi et al., 2020; Liu et al., 2013; Shebl et al., 2022, 2021b; Shebl and Csámer, 2021b) within the study district. Their results are checked using various analytical methods and field investigations to ensure the reliable output of the current study.

2. Geological Setting of the Study Area

Wadi Zayatit and Wadi Mikbi district is a part of the exposed Neoproterozoic basement rocks at the South Eastern Desert of Egypt and is delineated by Latitudes 24° 30' - 24° 06'N and Longitudes 35° 08' - 35° 15'E and covering an area approximately 200 Km^2. It is located at about 30 Km west of Gabal Hamata prominent village along Red Sea coastal plain and about 70 Km northwest of Bernice town. The height of Gabal Zayatit is 915 meters above sea level or 210 meters above the surrounding terrain. The highest point at the studied district is Gabal Mikbi; it has 1,370 meters above sea level, 5.7 Km west of Gabal Zayatit (Figs.1a&b). The studied district is totally covered by Neoproterozoic basement rocks of the Southern Eastern Desert. On the basis of previous geological maps, field observations, and previous works; different rock units are exposed in the studied district. The arrangement of the rock units, from oldest to youngest is the ophiolitic rocks (Serpentinites, metagabbros, amphibolites, and epidosite) along Wadi Zayatit and Wadi Mikbi district, the island arc assemblages, which is represented by arc-related metasediments (schists and quartzites), metagabbro-tonalite complex, Alaskan type intrusions (Dunite and olivine gabbros), and cordilleran stage represented by the granitic rocks. Wadi Zayatit and Wadi Mikbi district is injected by numerous dykes (Acidic and basic) and veins of different shapes and compositions invading all the different rock units cropping out in the study district (Figs.2a&b).

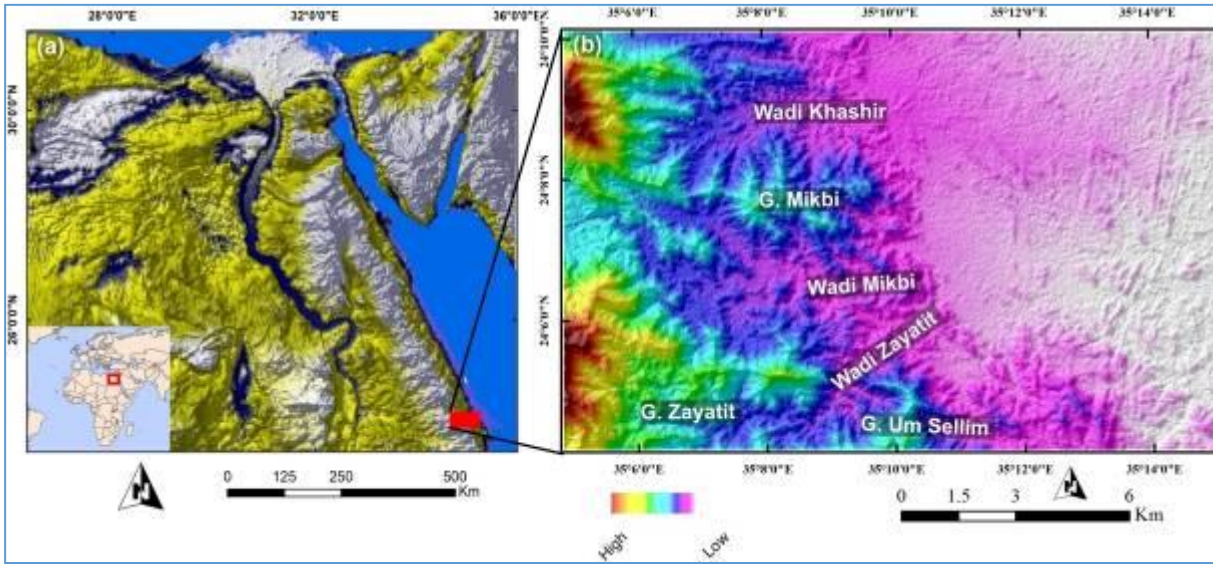

Fig.1. a) location map of the study district, b) ALOS PALSAR DEM of the study area, SED, Egypt

3. Materials and Methods

3.1. Remote Sensing Datasets

For the purpose of the current research, a terrain corrected (L1T), Advanced Spaceborne Thermal Emission, Reflection Radiometer (ASTER), and Sentinel 2A data were utilized. Incorporating these two multispectral datasets have proven its usefulness in various geological applications (Noori et al., 2019; Sekandari et al., 2020; Shebl et al., 2022, 2021a; Shebl and Csámer, 2021b, 2021c, Badawi et al., 2022, Abdelkader et al., 2022,). ASTER data provides a powerful short wave infrared range spectral coverage (Emam et al., 2016; Mars and Rowan, 2010; Pour and Hashim, 2012; Shebl et al., 2021a), and widely used in geological remote sensing. Sentinel 2 data introduce a higher spatial resolution (up to 10 m), besides its reliable results in lithological and hydrothermal alteration mapping (Cardoso-Fernandes et al., 2020; Drusch et al., 2012; Ibrahim et al., 2018; Mielke et al., 2014; Shebl et al., 2021b; Van der Meer et al., 2014). The detailed spectral and spatial characteristics of ASTER and Sentinel 2 data are summarized in table (1). ASTER data was atmospherically corrected by using FLAASH (Fast Line of sight Atmospheric Analysis to Hypercube), where Sentinel 2 data was preprocessed by using Sentinel Application Platform (SNAP) and QGIS software after excluding bands 1, 9, and 10 due to their coarse spatial resolution. For each dataset, the bands are stacked and prepared for applying various image processing techniques including False color combinations (FCC), Principal component analysis (PCA), Minimum noise fraction (MNF), constrained energy minimization and informative band ratios depending mainly on spectral characteristics of the target and band designations.

Table 1. Characteristics of the utilized remote sensing data.

ASTER			Sentinel 2		
Band	**Central wavelength (µm)**	**Spatial resolution (m)**	**Band**	**Central wavelength (µm)**	**Spatial resolution (m)**
1	0.560	15	1	0.443	60
2	0.660	15	2	0.490	10
3N	0.820	15	3	0.560	10
3B	0.820	15	4	0.665	10
4	1.650	30	5	0.704	20
5	2.165	30	6	0.740	20
6	2.205	30	7	0.782	20
7	2.260	30	8	0.842	10
8	2.330	30	8a	0.865	20
9	2.395	30	9	0.945	60
			10	1.375	60
			11	1.610	20
			12	2.190	20

For instance, visible and near-infrared (VNIR) bands are mainly utilized for detecting iron-bearing minerals while hydroxyl-bearing minerals are mainly sensed by using SWIR bands (Hunt, 1977; Hunt and Ashley, 1979). To perform a structural analysis by extracting linear features, Phased Array L-type band Synthetic Aperture Radar (PALSAR) data was implemented due to the efficiency of radar data compared to optical datasets in extracting lineaments (Shebl and Csámer, 2021c). PALSAR was mounted on the Advanced Land Observing Satellite (ALOS) that was launched in 2005 to provide higher resolution digital elevation mapping without being affected by weather conditions.

3.2. Field Evidence and Analytical Techniques

Using a global positioning system (GPS) survey, more than 120 rock samples were collected from the lithological units and alteration zones. Thin section preparation (for examination in the transmitted light), polished-thin section (for examination in the reflected light), X-ray diffraction (XRD) examination, and scanning electron microscope (SEM) investigations are implemented. A total of 45 thin sections collected from the investigated rock samples were analyzed petrographically under a polarized microscope to identify the mineral compositions, ore textures, and alteration types. Ore microscopy of the polished-thin sections, X-ray diffraction (XRD), and SEM-EDX techniques were used to identify the ore minerals, ore textures, and ore compositions. Scanning Electron Microscopy with EDX microchemical analyses were carried out on ore minerals in all samples by using SEM Model Quanta 250 FEG (Field Emission Gun) attached with EDX Unit (Energy Dispersive X-ray Analyses), at the Central Laboratories of the Egyptian Mineral Resources Authority (EMRA). The accelerating voltage was 30 kV, the magnification ranges from 14 x up to 1.000.000 x, while the resolution for the gun was 1nm.

4. Results and Discussions

4.1. Remote Sensing Results

4.1.1. Lithological mapping

To construct an updated lithological map**,** the remote sensing investigations by using ASTER and Sentinel 2 data has been utilized and revealed a reasonable lithological discrimination of the exposed rock units utilizing FCC, PCA, ICA, and MNF techniques as shown in figures (2, 3 & 4). Resolving

these different colors using remote sensing data only is a tedious task, thus together with the field observations and previous geological maps, all the remote sensing findings are interpreted helping in identification of serpentinites, ophiolitic metagabbros, amphibolites, epidosite, arc-related metasediments (schists and quartzites), metagabbro-tonalite complex, dunite, olivine gabbros, and granitic rocks. For instance, Sentinel 2 FCC (R: 12; G: 6: B: 2) also for other RGB (Figure 2a) separated felsic (granites) and mafic (gabbros) rocks in light and dark colors, respectively. This composite clearly demarcates gabbroic rocks at the central part of the study district in dark colors. These gabbroic rocks could be better specified by using Sentinel 2 PCA (R: 1; G: 2: B: 3) also for other RGB (Fig. 2b) into olivine gabbros (left dark pink color) and ophiolitic metagabbros (right light pink color) indicating the usefulness of embedding several techniques in lithological interpretations besides the fieldworks.

Similarly, Fig. 3a clearly discriminate olivine gabbros (dark blue color) from the ophiolitic metagabbros (light blue color) and demarcate granitic rocks in a reddish tone. Also, metagabbro-tonalite complex is clearly detected in light bluish strips trending WNW-ESE that is differentiated from olivine gabbroic rocks (dark blue color) of the extreme north western part of the study district. Inspecting figure (3b) allows clear identification of the granitic rocks (Biotite granites and deformed altered granites) in a green color that slightly differs in density according to slight mineralogical variances.

At the eastern part of the study district, deformed altered granites is intensively dissected by several dykes of various directions and highly weathered that's why a combination of colors could be seen within the deformed altered granites, however, the green hue still observed. Similarly, several colors interferences representing serpentinites, ophiolitic metagabbros, amphibolites, epidosite, arc-related metasediments (schists and quartzites), metagabbro-tonalite complex, and dunite are identified at the south western corner of the study district (Figs. 3 & 4). These findings are highlighted and used with the field observations in updating the lithological map of the study district. Through interpreting all of these results and field observations, a novel lithological map of the study district was introduced as shown in Fig. 5.

4.1.2. Structural mapping in relation to hydrothermal alteration types

The complicated color representations of the different rock units, and structural features, clearly indicate the existing hydrothermal alterations encountered in the study district. Thus the specific band ratios and constrained energy minimization techniques were adopted to reveal the alteration types recorded in the study district. The total hydrothermal alteration pattern is deciphered by using Sentinel 2 data by mimicking the well-known Sabins ratio (Sabins, 1997) for detecting the hydroxyl-bearing minerals, iron oxides, and ferrous iron oxides in RGB respectively as shown in figure (6a). The latter clearly demarcate the richness of gabbroic rocks by hydroxyl-bearing minerals and reasonable distribution of iron content over the granitic rocks besides ferrous iron dominated at the southern part of the study district associated mainly with serpentinites, ophiolitic metagabbros, amphibolites, epidosite, arc-related metasediments (schists and quartzites), metagabbro-tonalite complex, and dunite. Detailed inspection of each type of hydrothermal alteration was performed by specifying the target with the utilized spectral range of bands. For instance, ferrous iron content was separated by using Sentinel 2 band ratio 12/8 as shown in Fig. 6b). Its distribution considerably matches the result of Sabins ratio. Additionally, the distribution of ferric iron and hydroxyl-bearing minerals is given in Figs. 7a & 7b respectively. In Fig. 7b, the hydroxyl-bearing minerals are confined to gabbroic rocks and it intensively appears in the eastern part of the study district. The field observations of that part revealed that the dominant hydroxyl-bearing minerals of the eastern part are mostly resulting from weathering processes not hydrothermal alteration processes.

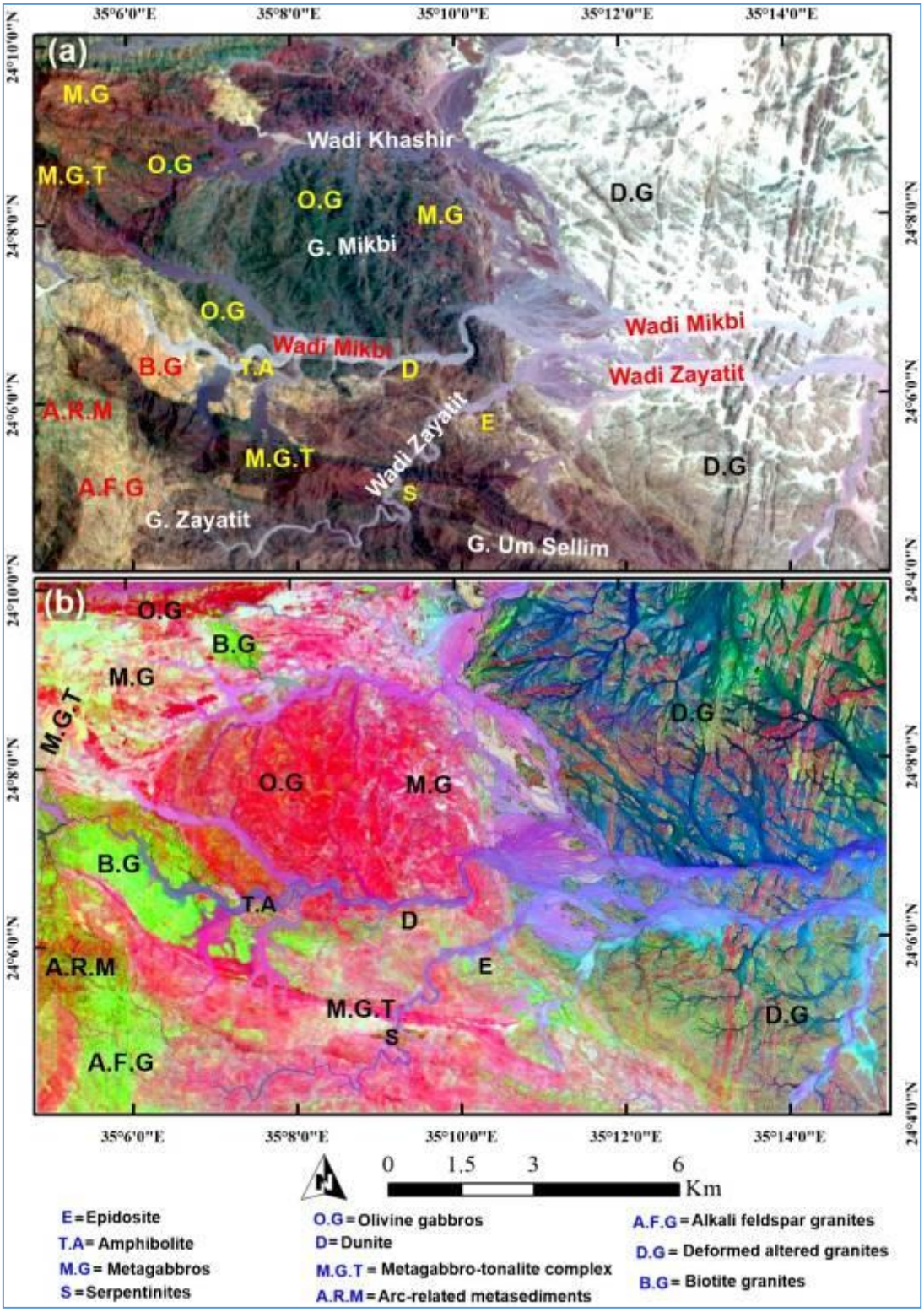

Fig.2. Lithological mapping by using Sentinel 2 data showing (a) FCC 12-6-2 in RGB and (b) PCs 1-2-3 in RGB respectively.

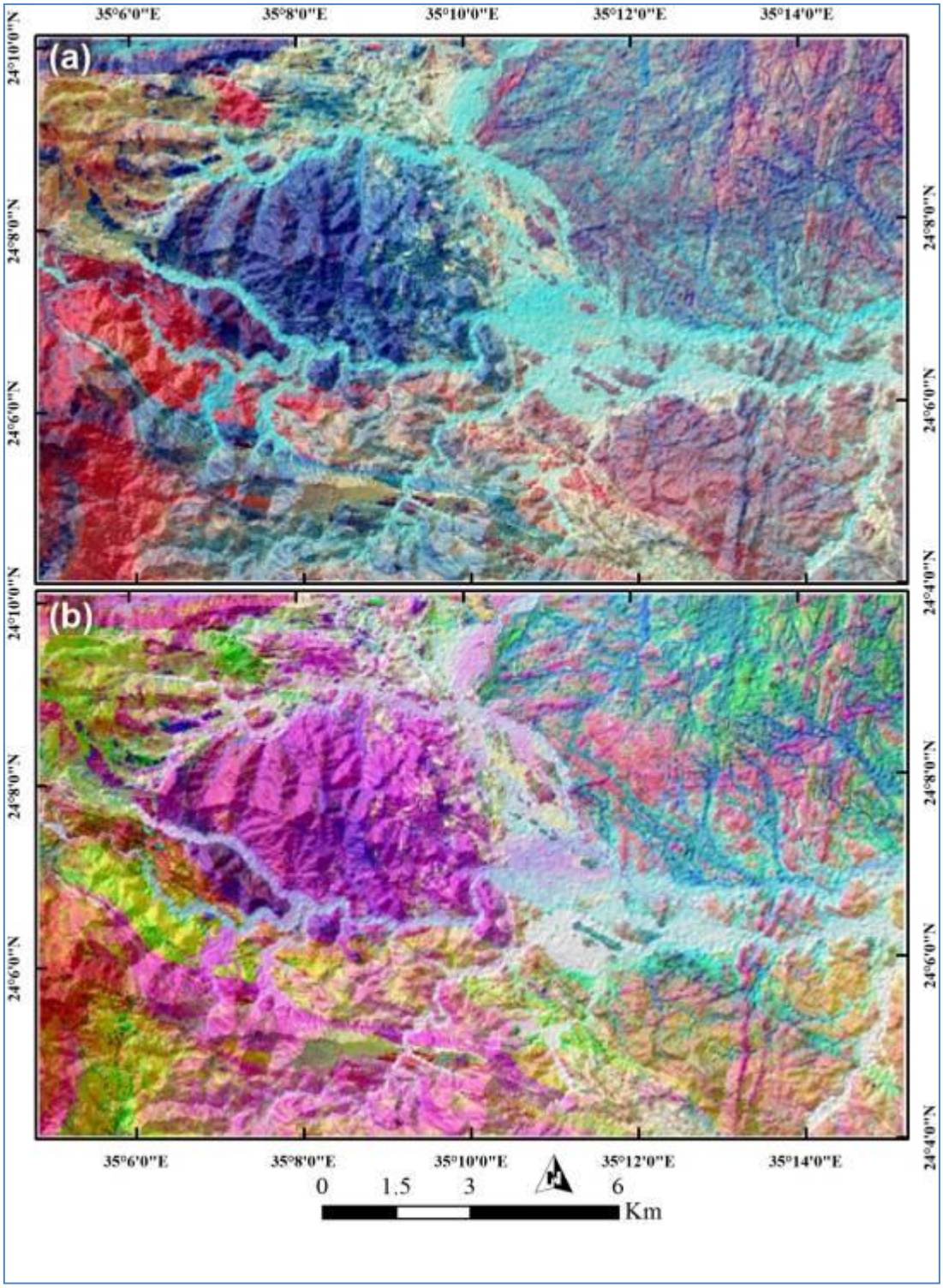

Fig.3. Lithological mapping by using Sentinel 2 data showing (a) PCs 2-3-4 in RGB and (b) ICs 3-1-2 in RGB respectively.

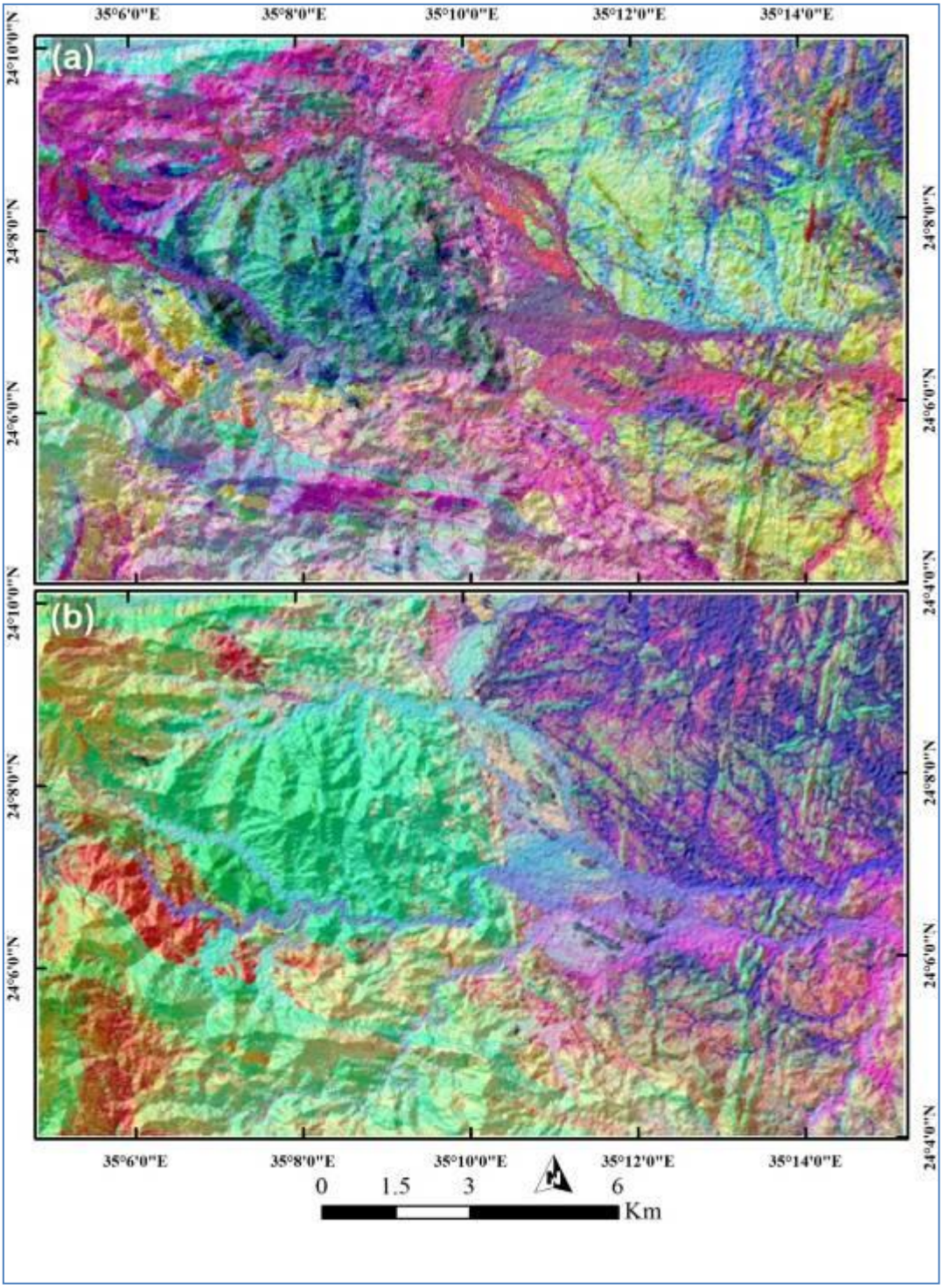

Fig.4. Lithological mapping by using Sentinel 2 data showing (a) MNF 2-4-5 in RGB and (b) MNF2-MNF1-PC4 in RGB respectively.

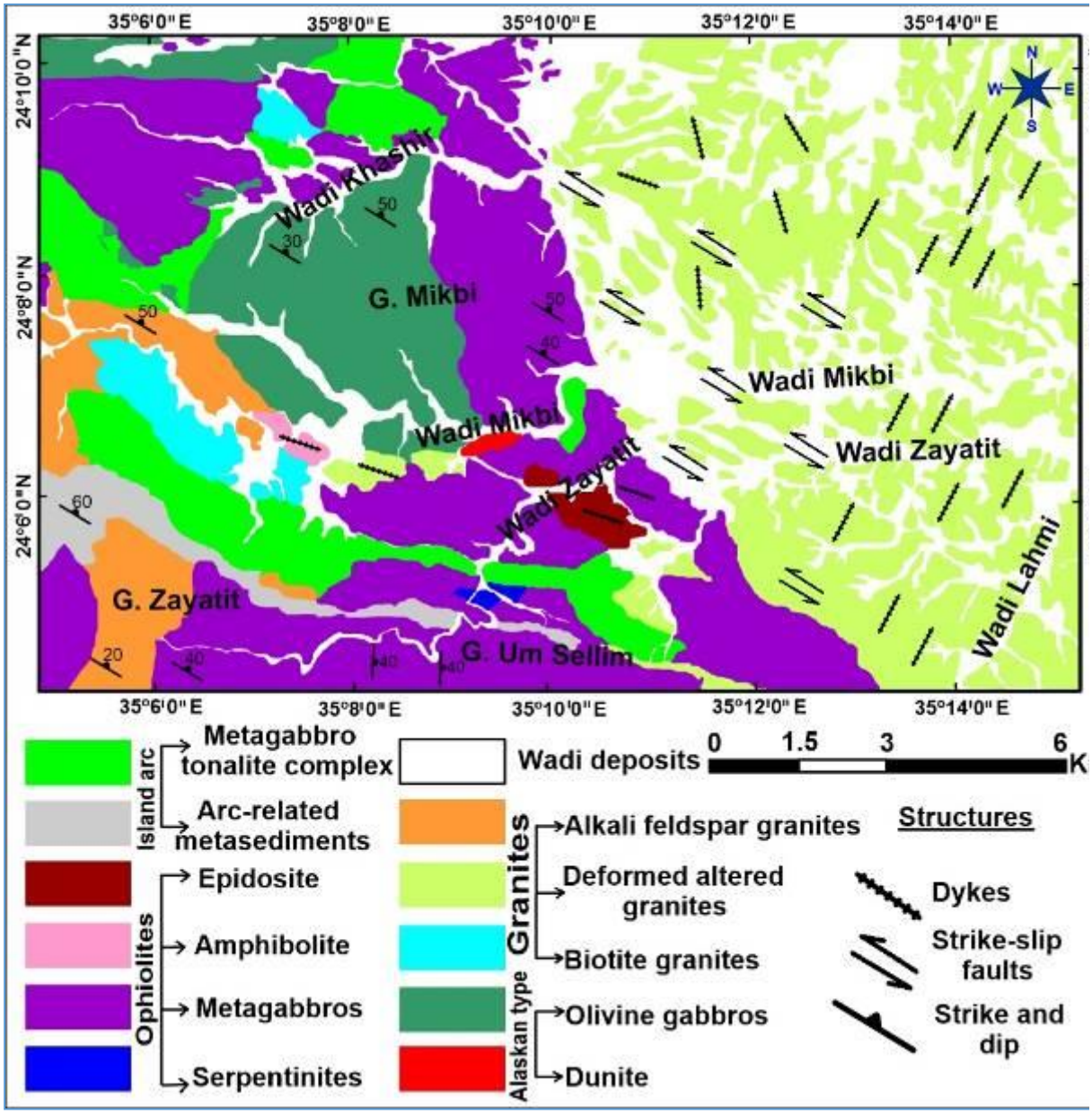

Fig.5. Detailed geological map of Wadi Zayatit and Wadi Mikbi district.

ASTER data was embedded in the hydrothermal alteration detection due to its detailed SWIR range allowing detection of specific minerals based mainly on the utilized wavelength and spectral libraries. For instance, gossan has been identified by using b4/b2 as shown in Fig. 8a. Indications for carbonate/chlorite/epidote content are given through spectral band depth (b7 + b9)/b8 as shown in Fig. 8b. Sericite/muscovite/illite/smectite content (b5 + b7)/b6 is revealed through ASTER data and revealed the effect of weathering processes on the eastern part of the study district (Fig. 9a), which is confirmed by detecting alunite/kaolinite/pyrophyllite content as shown in Fig.9b. ASTER ferrous (Fig.10a) and ferric (Fig. 10b) iron results show outstanding matching with Sentinel 2 findings and are confirmed during the field investigations.

Various mineralogical indices were also resolved by using ASTER thermal bands. For example, quartz, amphibolite, and muscovite contents are discriminated in RGB respectively in Fig.11a. Investigating the latter shows that a higher content of quartz and muscovite are almost associated with

the granitic rocks and amphibolite content is mostly associated with intermediate and mafic rocks. Towards specified detection of hydrothermally altered minerals, nine minerals were identified with the aid of the USGS spectral library by using a constrained energy minimization technique that has been widely utilized over similar terrains and provide reliable results (Aboelkhair et al., 2021; El-Magd et al., 2015; Shebl et al., 2021a). Results of CEM provide the distribution of chlorite, epidote, illite, pyrophyllite, kaolinite, montmorillonite, quartz, muscovite, and calcite (Fig. 11b). These minerals have been investigated to discriminate alteration-related from weathering products and confirmed by using the field investigation and laboratory studies. Comprehensively and with reference to the field observations, remote sensing results indicated that several types of hydrothermal alteration are represented within the study district, however, the oxidation process is considered the dominant type.

Besides lithological mapping and hydrothermal alteration detection, remote sensing data (ALOS PALSAR DEM) introduced a reasonable outline for the structural features within the study district. These structural elements have a considered role (pathways for hydrothermal solutions) in controlling various metallic mineral deposits. Thus, PALSAR DEM was used as an input for PCI Geomatica software to extract lineaments and highlight highly dissected zones by specifying various parameters including filter radius (10), Edge Gradient Threshold (50), Curve Length Threshold (30), Line Fitting Threshold (3), Angular Difference Threshold (15), and Linking Distance Threshold (20).

The present results revealed that the study district is mostly dissected with NW-SE trending lineaments. A lineament density map was constructed to detect highly dissected zones that are of the utmost importance (together with the distribution of hydrothermal alteration zones) for detecting the mineral deposits. The lineament density map highlighted (Fig. 12) several structural anomalies on the western side of the study district besides manifesting the deformed altered granites in the eastern part of the study district as a highly dissected zone (which is totally coinciding with the field observations especially with the dykes at the eastern part of the study district).

4.2.1. Field verification

A field observation was carried out to confirm the lithological discrimination by using remote sensing data, verify the newly-constructed lithologic map and check the properties of alteration zones, and structures. Coinciding with remote sensing findings, a thorough field observation showed that the ophiolitic rocks (serpentinites, metagabbros, amphibolites and epidosite) are mainly distributed along Wadi Zayatit and Wadi Mikbi. For instance, several scattered slices of serpentinites are encountered (in the central southern part of the map) within the ophiolitic metagabbros that are exposed dominantly at Wadi Zayatit. They occur as lens-like bodies or shear pods within the enclosing rocks (Fig. 13a). These lenses vary from 20 to 50 m in length and from 10 to 20 m in width. In general, they show dark green and grey colors, in places these rocks are quite massive, sheared, sometimes transformed to talc-carbonate rocks and the presence of small magnetite crystals along the shear zones.

Similar to its slightly-varied colors in remote sensing results, field observations of the ophiolitic metagabbros show wide variations in color, which ranges from dark green to dark grey and include two main varieties. The first variety exhibits small scale rhythmic layering, whereas, the second one is coarse-grained with hypidiomorphic granular texture and consist mainly of pyroxene and/or amphibole and plagioclase. Rhythmic layering is well developed, where leucocratic layers sharply alternate with dark layers and their thickness range from 1 to 10 cm. Titanomagnetite crystals recorded in the ophiolitic metagabbros are occasionally observed during the field investigations (Fig. 13b). The amphibolites show polyphase deformation but they are generally brittle deformed and contain linear zones of strongly foliated banded gneissic gabbroic amphibolites. The amphibolites can be traced into undeformed gabbros. The field observation may suggest that the amphibolites were derived from gabbroic protoliths

and related to regional fault zones (Fig. 13c). There are small titanomagnetite and magnesioferrite crystals found in some amphibolite samples.

Additionally, the epidosite was detected in the field observations as yellowish brown and grey colors. The epidosite is known to be hosted by the South Eastern and central parts of the mapped district (epidotized rocks exposed at Wadi Zayatit encountered in the metagabbro-tonalite complex).

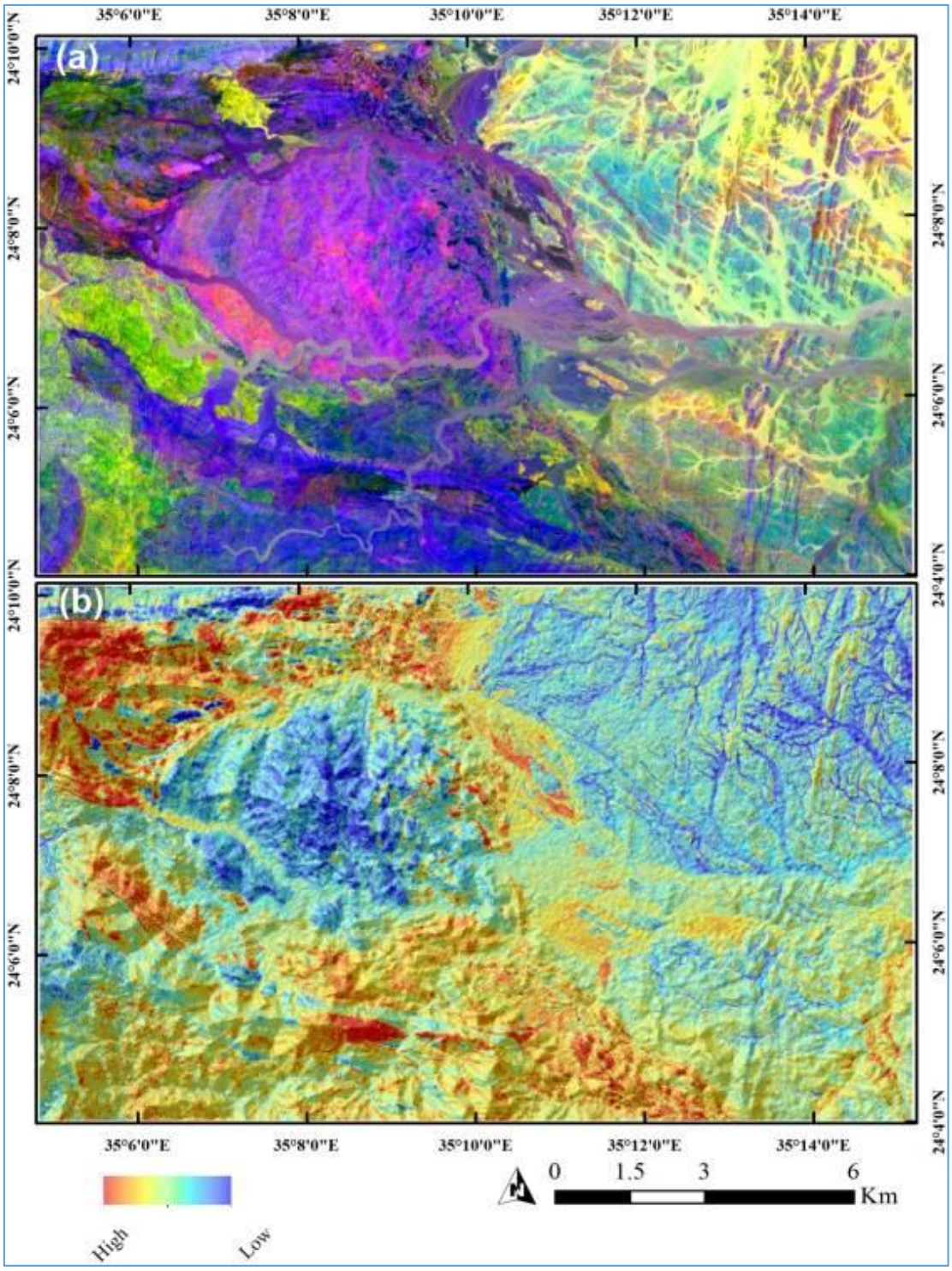

Fig.6. Hydrothermal alteration delineation by using Sentinel 2 data showing (a) Sabins ratio and (b) ferrous iron distribution**.**

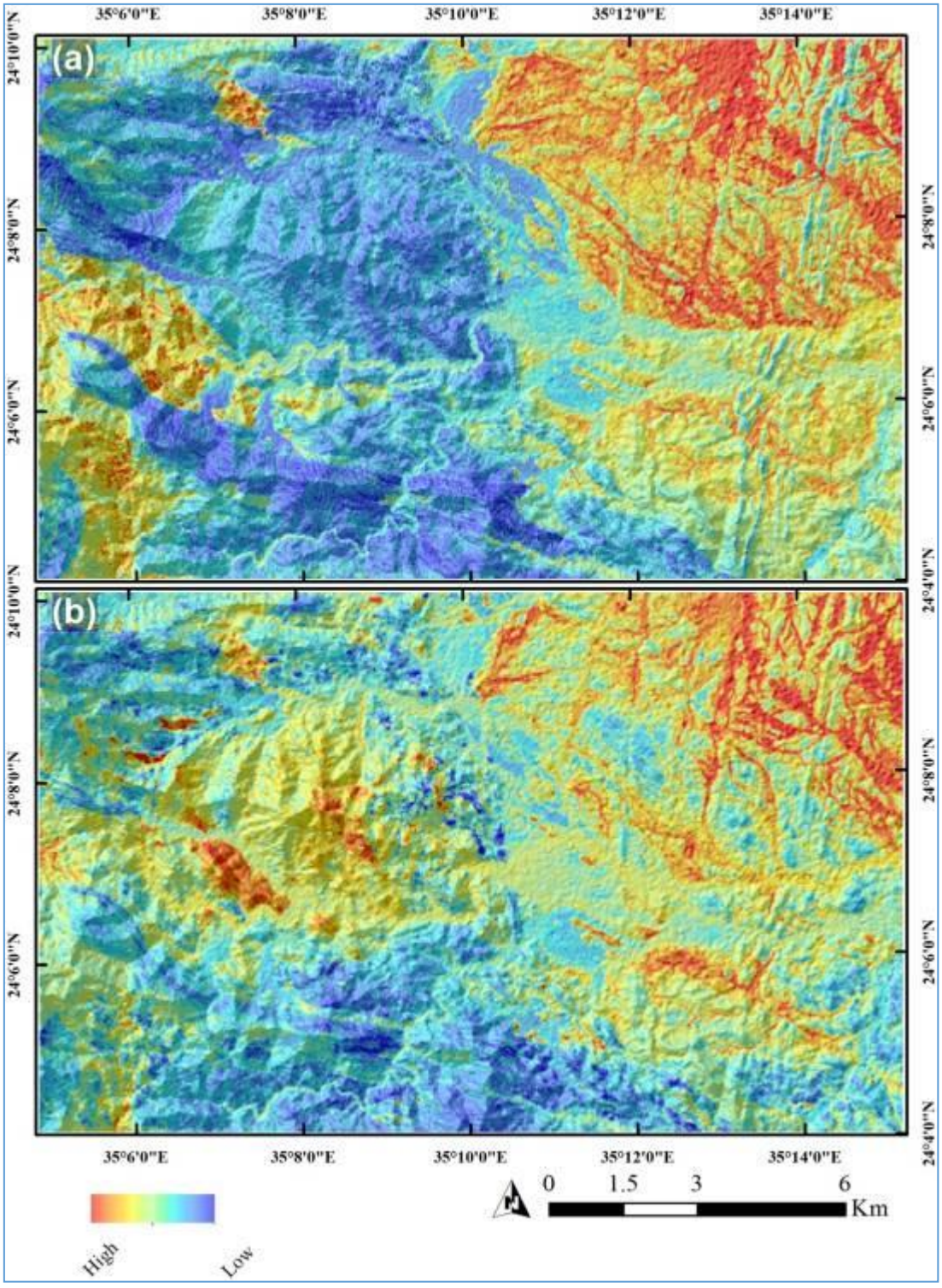

Fig.7. Hydrothermal alteration delineation by using Sentinel 2 data showing (a) general iron distribution and (b) hydroxyl bearing minerals within the study district.

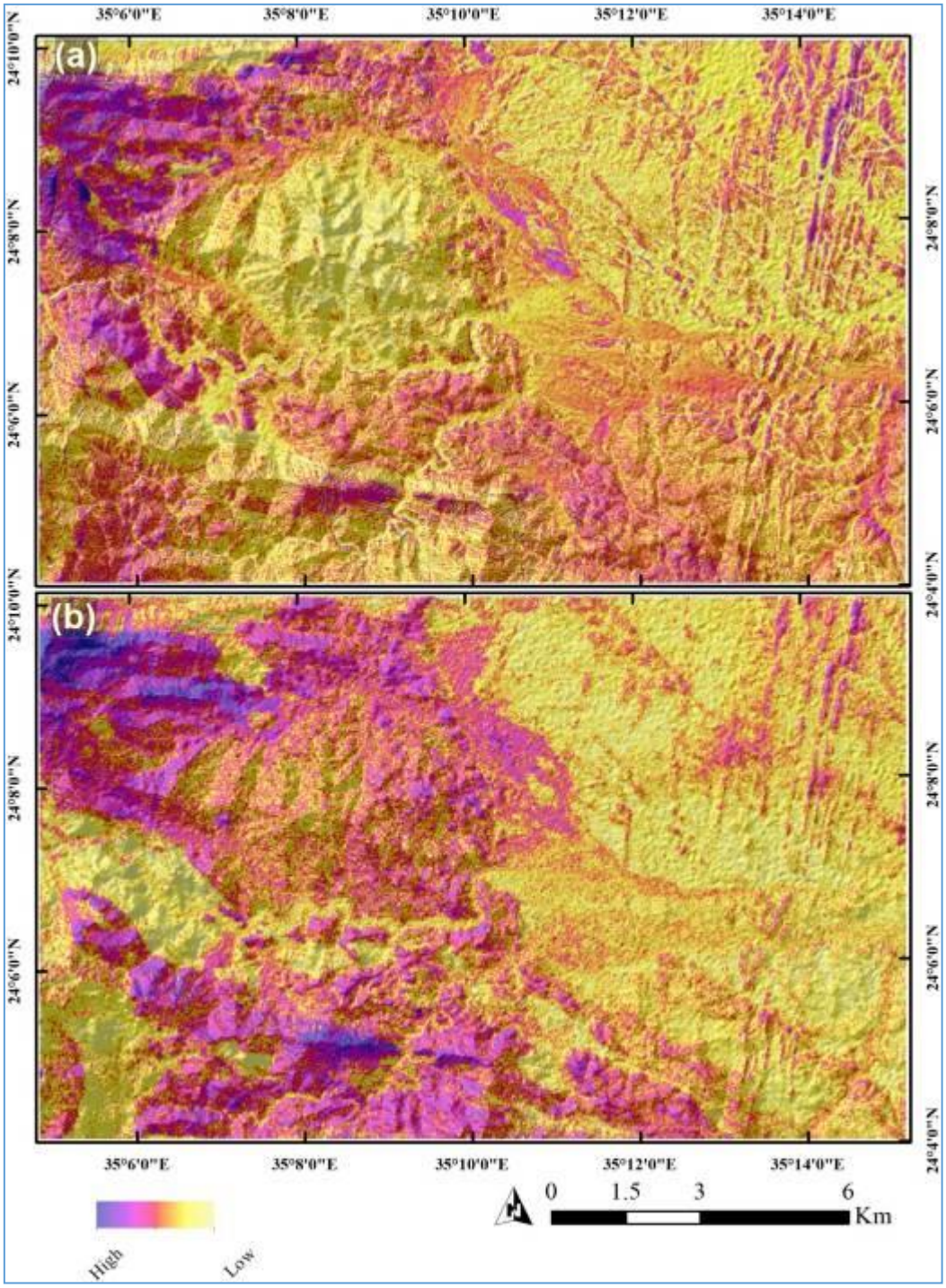

Fig.8. Hydrothermal alteration delineation by using ASTER data showing (a) gossan and (b) carbonate/ chlorite /epidote rich zones.

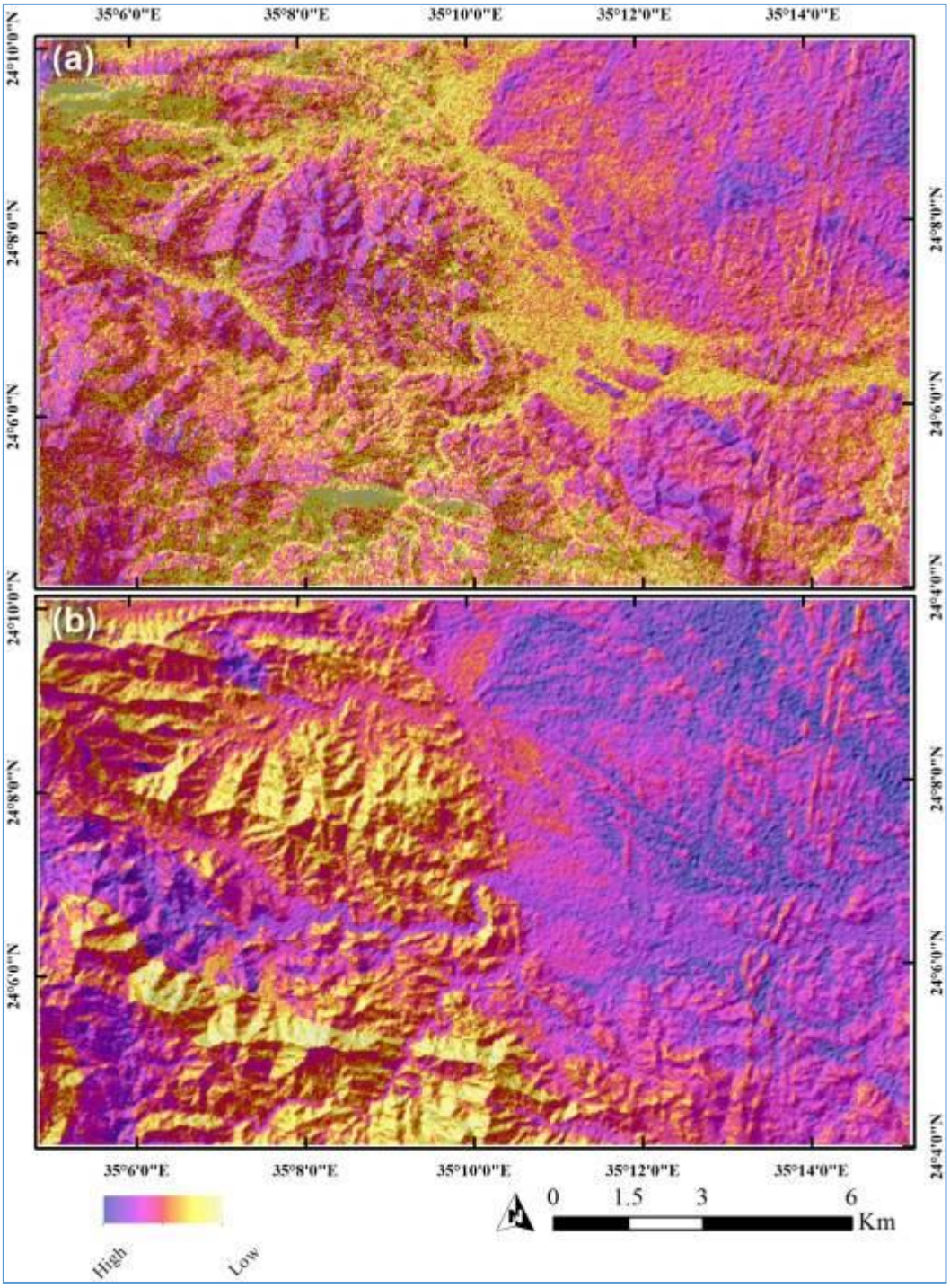

Fig.9. Hydrothermal alteration delineation by using ASTER data showing the distribution of (a) muscovite/sericite/ illite and (b) alunite/kaolinite/pyrophyllite.

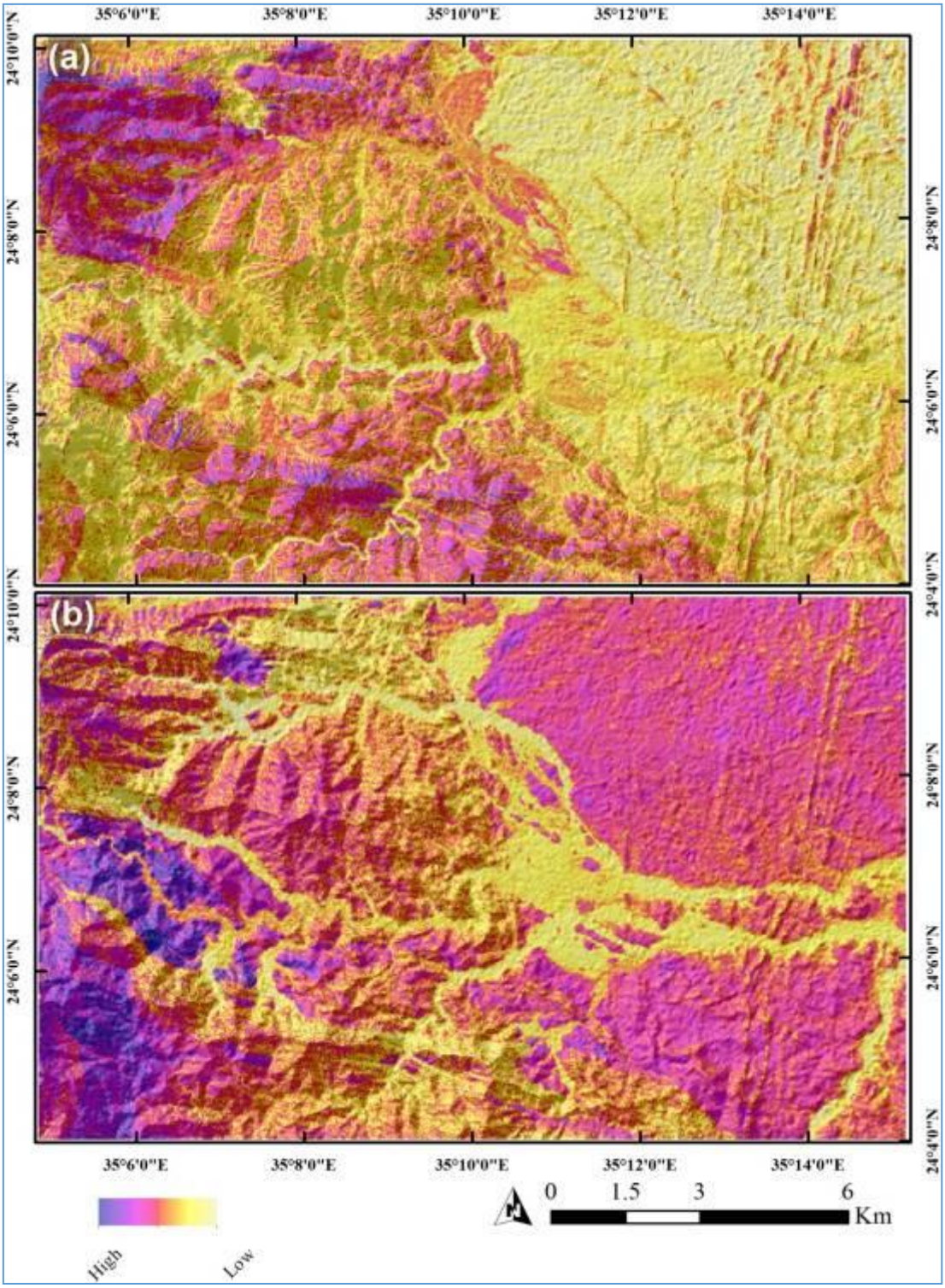

Fig.10. Hydrothermal alteration delineation by using ASTER data showing (a) ferrous and (b) ferric iron distribution.

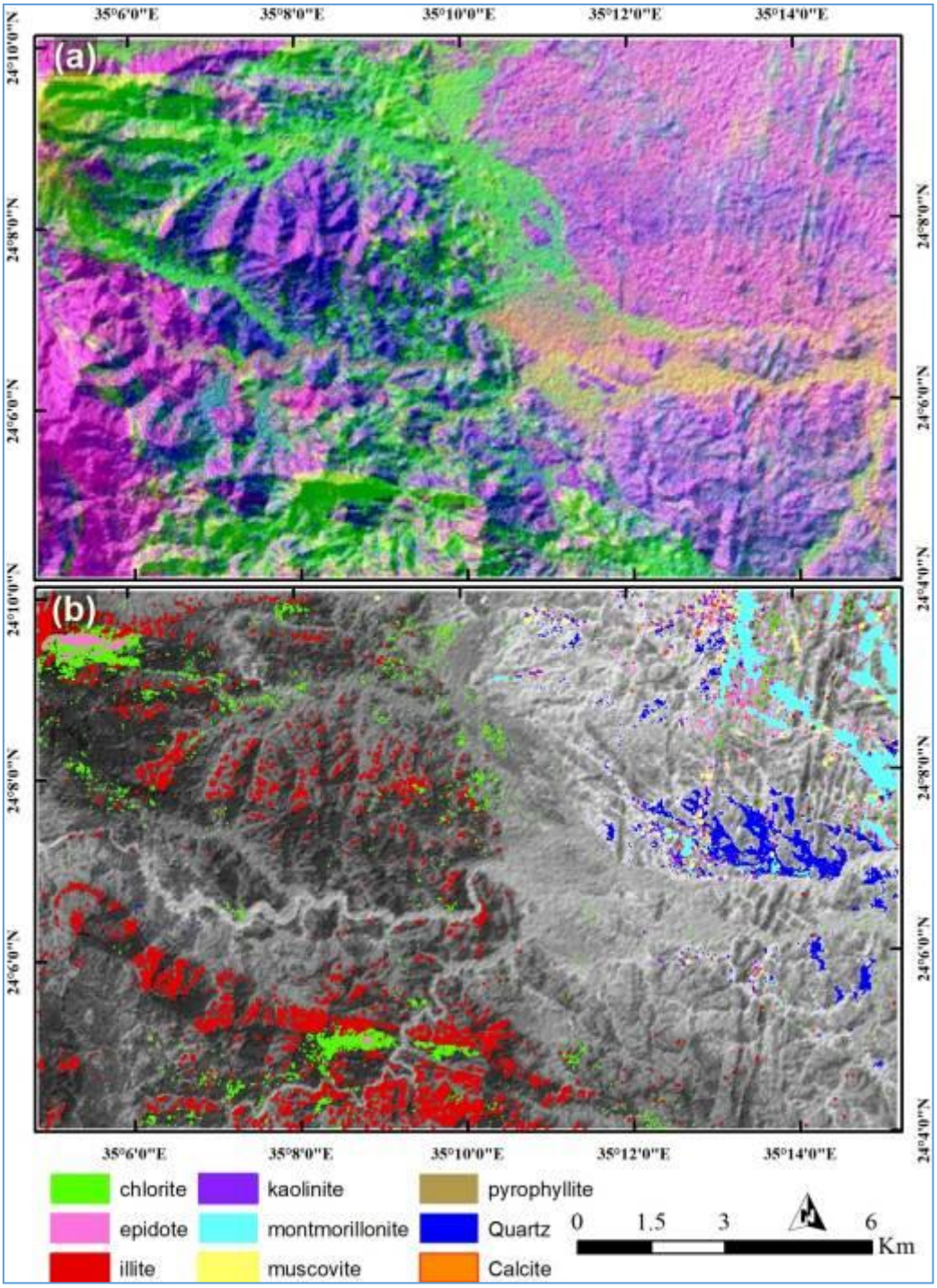

Fig.11. Hydrothermal alteration delineation by using ASTER data showing the distribution of (a) quartz (red) amphibole (green) and muscovite (blue) and (b) CEM results.

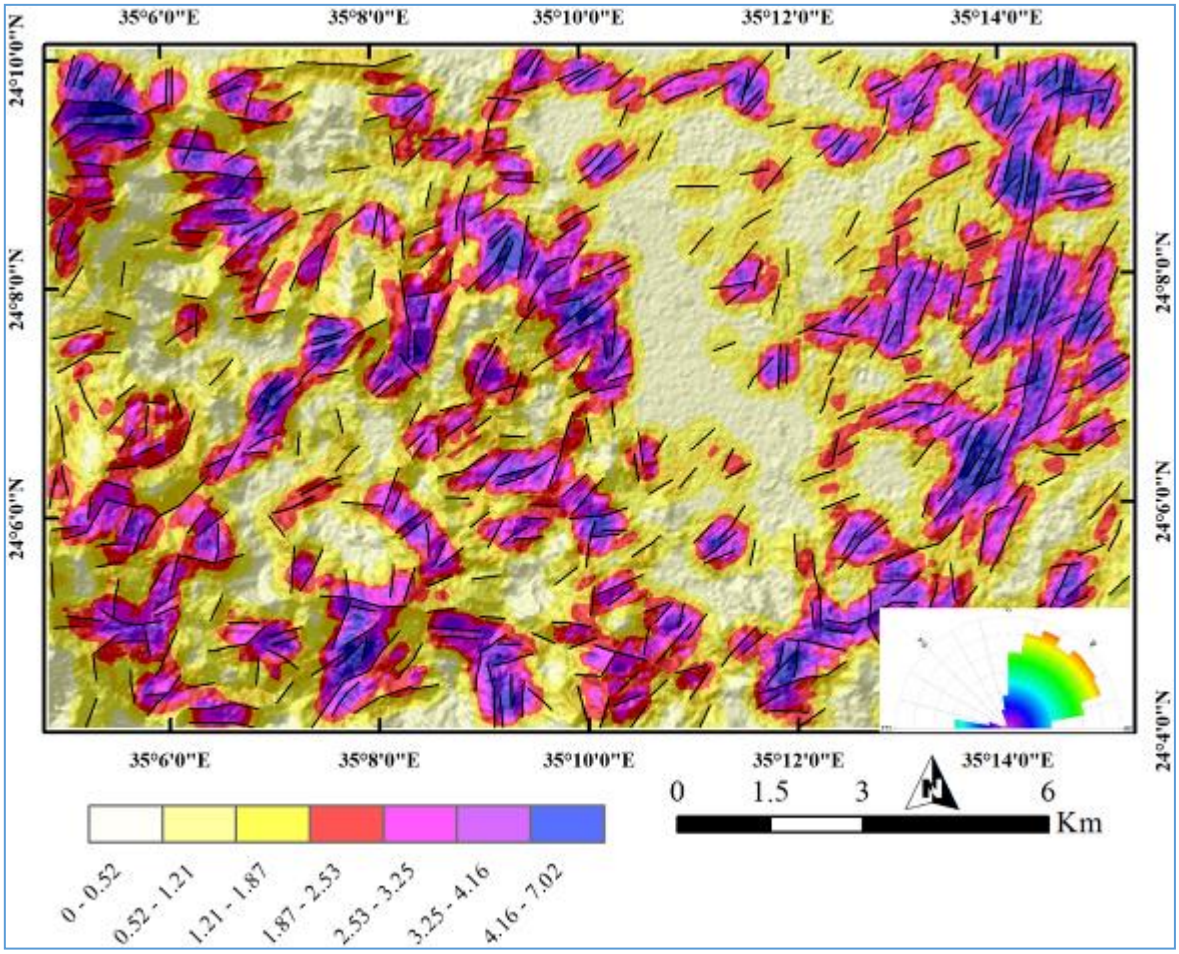

Fig.12. Lineament density map of the study district.

The epidosites may occurs as fracture controlled, spotty alterations emplaced at metagabbro-tonalite complex (in this case, it must be younger than this family of intrusions) or sheeted dikes epidosite generations (recorded in Wadi Zayatit within the ophiolitic metagabbros). This assumption seems to be reasonable, because all the late alteration in fact displays pervasive chlorite-albite-quartz alteration of the metagabbros, which proves they were permeable to hydrothermal solutions (Fig. 13d).

According to the remote sensing findings, the arc-related metasediments (schists and quartzites) are highly deformed, foliated, schistose, and folded as well as recorded mainly in the southwestern part of the study district. These rocks are confirmed by the field observations and cropped out mainly around the whole mass of the gabbroic rocks expect its eastern side. In general, the studied schists are fine- to coarse-grained, show variation in colors ranges from yellow to brown and sometimes grey to dark grey. These rocks have sharp contact with the ophiolitic foliated metagabbros. Generally, these rocks are quite massive occasionally foliated a schistose (detected by remote sensing data and field study), and transformed to chlorite-actinolite schists and quartzites (Fig. 13e & f).

Metagabbro-tonalite complex, these rocks form moderately continuous rugged ridges and are mainly encountered in the central southern part of the study district. The metagabbros are intruded by granitic rocks, and that carry xenoliths of this metagabbros within the gneissic tonalite (Figure 14a & b). Most of them are parallel to the foliation of metagabbros. Wadi Zayatit and Wadi Mikbi provide a good section across the metagabbro exposure. In the east and west, these metagabbros are clearly intruded by granitic rocks at the northern and western parts. The small elongated belt of the metagabbro-tonalite complex occurs either as boulders, medium to high hilly masses dissected by many joint trends at Wadi Zayatit and Wadi Mikbi. It is massive, slightly deformed and shows moderate relief found or

has sub-circular or irregular plutons. Generally, these rocks are dissected by a number of tonalite sheets and albite dykes (Fig.14c & d).

Dunite, the lower crustal part of the Alaskan type intrusion consists of metagabbros. These are in turn intruded by late intrusive dunite bodies and presence of small black chromite crystals. Field relationships shows these dunite bodies do not show intrusive contacts with the foliated ophiolitic metagabbros (Fig. 14e).

Olivine gabbros, they exposed in the NW and W of Wadi Mikbi district. They exhibit dark greenish grey in fresh surface, with lustric features, massive, and slightly deformed and easily discriminated in remote sensing data (Fig. 2). It sometimes forms spheroidal weathered masses, and composed essentially of medium- to coarse-grained of olivine and plagioclase crystals. The average thickness of olivine gabbros ranges from 5 to 15m (Fig. 14f).

Based on remote sensing data (Figs. 2, 3, & 4), three main varieties of late- to post-orogenic granites are identified as biotite granites, alkali feldspar granites, and deformed altered granites. These rocks crop out in eastern and western parts of the mapped area. These rocks are well developed in the western part of Wadi Mikbi and occur as strongly foliated biotite granite sheets encountered in the gabbroic rooks. Scattered subrounded to angular gabbroic xenoliths less than 20cm across are observed in these rocks. These rocks exhibit boulder weathering and exfoliation medium- to coarse-grained grey to whitish grey in color (Fig. 14g & h).

Wadi Zayatit and Wadi Mikbi district is injected by numerous dykes and veins of different shapes and composition invading all the rock units cropping out at the study district. This dyke of the study district is represented by basic and acidic dykes running in NW – SE direction through the northern and eastern parts of the mapped area (Fig. 14i). All of these rock units and dykes show a considerable matching in their spatial distribution with remote sensing lithological discrimination findings.

Special interest was given during the field investigation to emphasizing the hydrothermal alteration zones and comparing them with those detected by using ASTER and Sentinel 2 data. In a harmony with remote sensing findings, oxidation, epidotization, carbonatization, chloritization, silicification, phyllic, propylitic, and argillic alterations were detected. The oxidation alteration zones were found in relation to the iron ore mineralization that associated with the most rock units of the study district (Fig. 13 & 14) such as serpentinites (Fig. 13a), ophiolitic metagabbros (Figure 13b & d), amphibolites (Fig. 13c & d) metagabbro-tonalite complex (Fig. 14a, b, c & d), dunite (Figure 14e), olivine gabbros (Fig. 14f), granitic rocks (Figs. 13d, 14g & h), and dykes (Fig. 14d & i).

The present investigations revealed that the prevalent alteration type is oxidation and its associated mineral deposits are hosted mainly in the ophiolitic rocks and island arc assemblages. To confirm these hydrothermal alterations and their related ores and verify the remote sensing distribution maps and the field observations, a detailed petrographical and mineralogical analysis was performed.

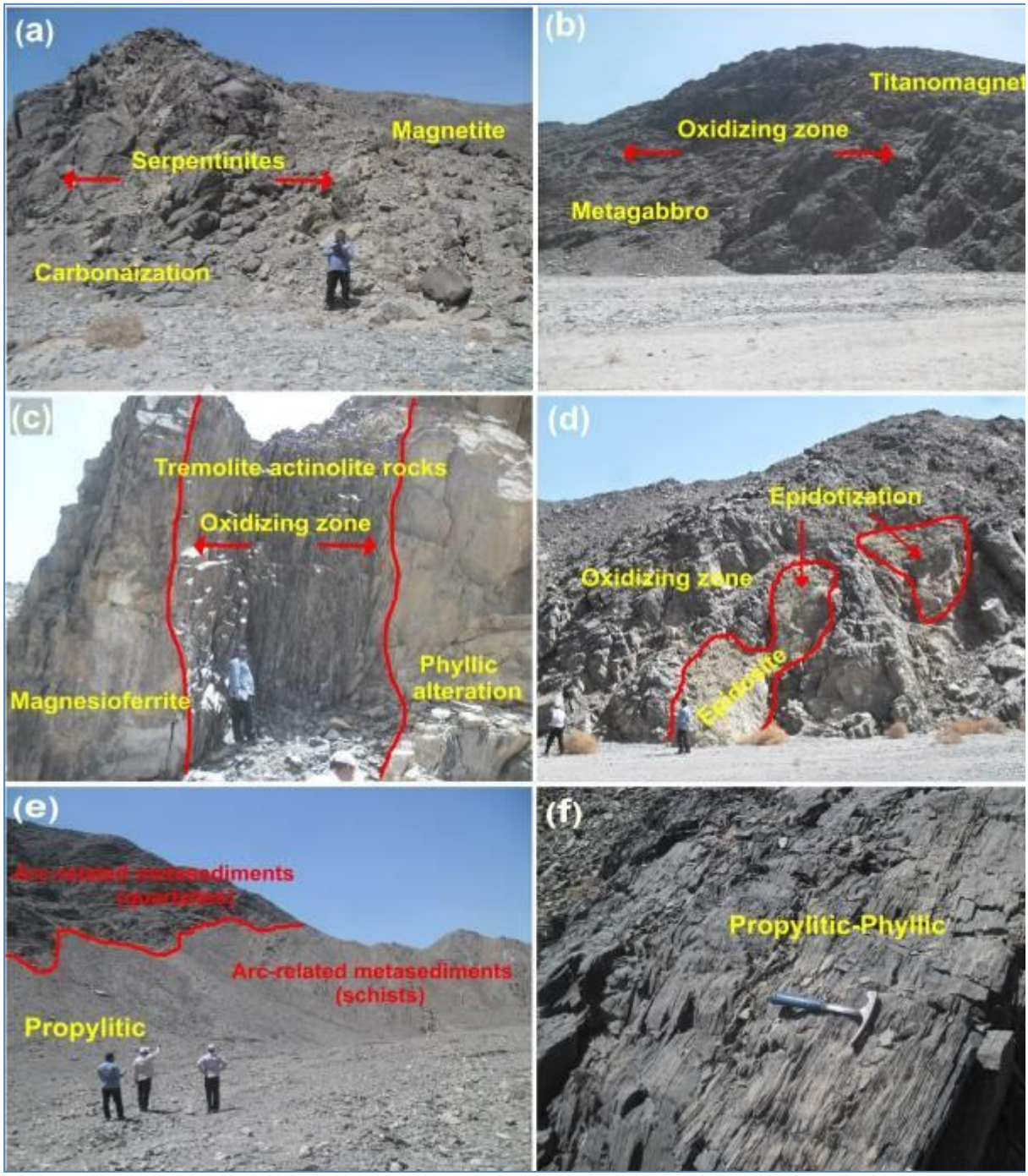

Fig.13. Field observations of some hydrothermal alteration zones encountered in the study district: (a) Magnetite-bearing carbonatization zone present in serpentinites. (b) Titanomagnetite crystals-bearing the oxidizing zone encountered in the ophiolitic metagabbros. (c) The oxidizing zone-bearing the phyllic alteration associated with magnesioferrite crystals that encountered in the amphibolites. (d) Epidotization alteration-bearing the oxidizing zone found in the ophiolitic metagabbros. (e) Propylitic-Phyllitic alterations associated with the arc-related metasediments of schists and quartzites. (f) Propylitic-phyllic alteration zones associated with the arc-related metasediments.

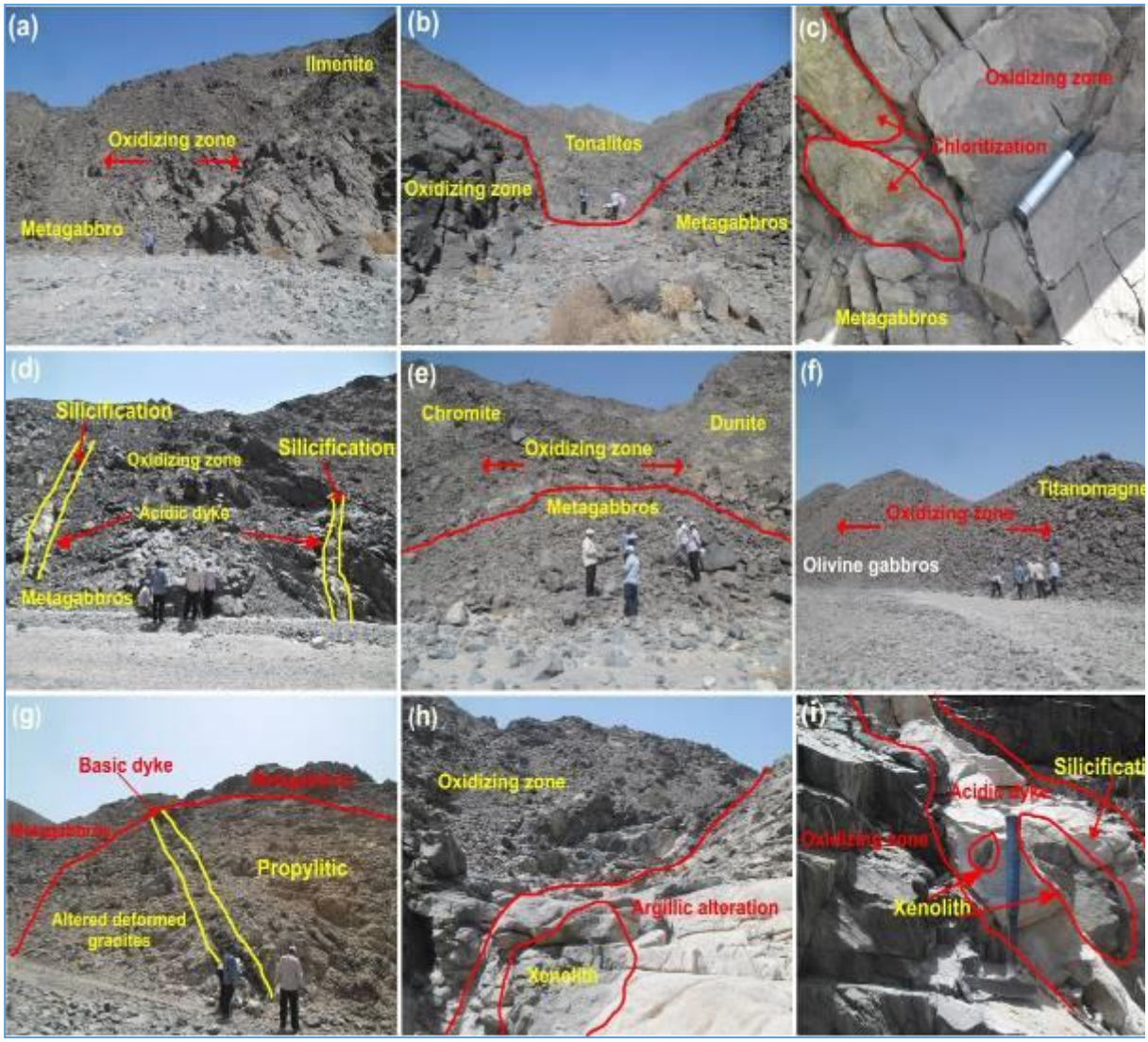

Fig.14. Field observations of the hydrothermal alterations in the study district showing: (a) Ilmenite-bearing the oxidizing zone encountered in the metagabbro-tonalite complex. (b) Oxidization alteration present in the metagabbro-tonalite complex. (c) Chloritization alteration adjacent with the oxidizing zone that found in the ophiolitic metagabbros. (d) Silicification alteration adjacent with the oxidizing zone encountered in the acidic dykes that found in the ophiolitic metagabbros. (e) Chromite-bearing the oxidizing zone present in dunite. (f) Titanomagnetite-bearing the oxidizing zone found in the olivine gabbros. (g) Propylitic alteration-bearing the oxidizing zone encountered in basic dykes that found the ophiolitic metagabbros and granitic rocks. (h) Argillic alteration-bearing the oxidizing zone adjacent with the shear zone between the ophiolitic metagabbros and the granitic rocks associated with xenoliths. (i) Silicification alteration-bearing oxidizing zone and xenoliths that invaded by acidic dyke, which encountered in the ophiolitic metagabbros.

4.2.2. Petrography of hydrothermal alteration processes

Wadi Zayatit and Wadi Mikbi Neoproterozoic basement rocks affected by some alteration processes observed in the studied district. These alteration processes include oxidization, phyllic, serpentinization, carbonatization, epidotization, silicification, zoisitization, muscovitization, sericitization, and chloritization (Fig. 15).

Oxidization zones are the most important oxide minerals encountered in the studied Wadi Zayatit and Wadi Mikbi rock units. Oxidization process recorded in the studied iron-bearing serpentinites,

dunite, ophiolitic metagabbros, olivine gabbros, metagabbro-tonalite complex, and amphibolites. It is black and dark black in color, and may cement to form subsurface iron rust found in these oxidation zones (Fig. 15a). The phyllic alteration is characterized by the completely replaces the potash feldspars and plagioclase by sericite that found in the amphibolites (Fig. 13c). **S**erpentinization process is the hydrothermal alteration by which magnesium-rich silicate minerals converted into or replaced by serpentine minerals. Serpentinization process is the most common type of alteration of the ultramafic rocks (Figure 15a). Serpentine minerals (antigorite, chrysotile, lizardite, and enstatite) are formed from olivine and pyroxene by the introduction of copious amounts of H_2O and CO_2 with an exothermic reaction (Pirajno, 2009). A typical example is the conversion of olivine to serpentine, according to the following equation:-

$$2Mg_2SiO_4 + H_2O + 2H^+ \rightarrow Mg_3Si_2O_5(OH)_4 + Mg^{+2} \quad (1)$$

Olivine serpentine

Serpentinites of the ophiolitic ultramafic rocks contain the assemblage of antigorite, enstatite, magnetite, and chromite. The latter is a common by product of serpentinization and is due to expulsion and oxidation of Fe from the silicate lattice. Serpentinites is extremely ductile and is easily transported during tectonic movements. Serpentinization of the ultrabasic rocks in which the serpentine minerals were replaces olivine in the serpentinites. Carbonatization process is the changes observed in the rocks leading to the formation of calcium, magnesium, iron, and manganese carbonates. The study serpentinites and amphibolites frequently undergoing carbonatization under the action of hydrothermal solutions rich in carbon dioxides (Figs.13a & 15c). Epidotization is the transformation process during which epidote originates at the expense of plagioclase crystals. Epidotization recorded in the most rock units of the study district such as epidosite, ophiolitic metagabbros, arc-related metasediments, metagabbro-tonalite complex and granitic rocks (Figures 13d & 15d). Zoisitization process formed from calcium-bearing plagioclase crystals that altered to zoisite. The zoisitization will be spread through the plagioclase crystals or near its outer margins. Zoisite is present as alteration products within a plagioclase crystal observed in the ophiolitic metagabbros (Fig.15F), epidosite, and amphibolites. They are often grown as layers along cleavages of the hosted plagioclase crystals. Muscovitization process is mainly after potash feldspars and albite plagioclase crystals recorded in the granitic rocks (Fig. 15g) and represented by large crystals occupying the interstitial spaces between plagioclase, and quartz. They are also present as fine inclusions in the feldspar crystals effect of alteration processes. Muscovite found in the studied granites follows the equations of Munha et al. (1980) given below is generally derived from albite and K-feldspar: -

$$3NaAlSi_3O_8 + K^+ + 2H^+ + 12H_2O \text{ (Albite)} \rightarrow KAl_3Si_3O_{10}(OH)_2 + 3Na+ + 6H_4SiO_4 \quad (2)$$

$$3KAlSi_3O_8 + 12H_2O + 2H^+ \text{ (K-feldspar)} \rightarrow KAl_3Si_3O_{10}(OH)_2 + 2K^+ + 6H_4SiO_4. \quad (3)$$

Sericitization process was formed in which potash feldspars and plagioclase crystals and other minerals are replaced by sericite through the action of low-temperature hydrothermal solutions on the rocks. Sericitization of plagioclase is well-developed in all the Wadi Zayatit and Wadi Mikbi Neoproterozoic basement rocks, but is most characteristic of the granitic rocks (Fig. 15h). The sericitized shear zones may have formed when partially silicified rocks were sheared (Harlov and Austrheim, 2013). Kaolinitization is transformation of aluminosilicates to kaolin in the acidic igneous rocks (granites). Kaolin results from kaolinitization, the process of alteration of the feldspars in the hydrothermal alteration process. Kaolinitization is also locally concentrated due to which potash feldspar crystals are represented by massive kaolin pseudomorphs (Fig.15e). The silica and potassium oxides are washed away leaving behind the kaolin. The petrographic investigation reveals that this process observed in the granitic rocks. Kaolinitization process formed as a result of the alteration of alkali feldspars into the kaolinite mineral under slightly acidic solutions. Surface waters readily dissolve

carbon dioxide (CO_2) from the chemical weathering of the granitic rocks (Pirajno, 2009). Potash feldspars are altered to kaolinite in the presence of carbonic acid and water, with potassium ion, bicarbonate, and silica in solution as byproducts (Fig. 15h). The alteration of alkali feldspars into the kaolinite under slightly acidic solutions by fresh water (rain water is the cause the alteration of plagioclase to kaolinite) in supergene conditions. Chloritization process was observed as replacements of ferromagnesian minerals. Chlorite phases replace some biotite and hornblende crystals in the different types of the granitic rocks, metagabbro-tonalite complex, amphibolites, ophiolitic metagabbros, and arc-related metasediments (Figs. 14c & 15i). These chlorites can be crystallized at temperature ranges from 250°C to 290°C, assuming a constant pressure of 1 kb (Walshe, 1986). Ford and Green (1977) envisage a largely meteoric hydrothermal origin for the propylitic alteration assemblages at temperature of 200°C.

Silicification process is used to describe a rock in which the silica content is increased by the metasomatic alteration. The metasomatic quartzification is obviously of hetero-oriented replacement pattern because the crystallographic lattice of the quartz is completely different from that of the feldspar being replaced (Pirajno, 2009). Silicification alteration spatially associated with the alteration zones, generally formed as replacements along mineralized hydrothermally altered granitic rocks, ophiolitic metagabbros, acidic dykes, and metagabbro-tonalite complex (Figs. 14d, 14i & 15e). Propylitic alteration is comprises mainly epidote and chlorite, together with lesser amounts of zoisite and calcite (Figs. 14e & f). Argillic alteration affects largely plagioclase feldspars, which is characterized by the formation of clay minerals in the granitic rocks (Fig. 14g & h). Twenty-five thin-polished sections were prepared from selected samples for ore microscopy by using a reflected light microscope, X-ray diffraction (XRD), and scanning electron microscope technique (SEM/EDX).

4.2.3. Paragenetic sequence of the mineral deposits

Mineral deposits exhibit complex paragenesis in which multiple episodes of metamorphism, magmatism, oxidation and supergene solutions are evident. The mineral deposits at Wadi Zayatit and Wadi Mikbi district exhibit both lithological and structural controls. The ore minerals are commonly crystalline aggregates along alteration zones, dykes, fractures, irregular masses, and disseminated oxides deposits are the common types of the ores in the studied district. Paragenetic sequence of Wadi Zayatit mineralization shows early metamorphic minerals of the arc-related metasediments. The early metamorphic mineral deposits chlorite is characterized by low- to medium-grade regional metamorphism of greenschist facies while irregular patches, veinlets and disseminated textures. Generally, magnetite, ilmenite, titanomagnetite, chromite and magnesioferrite are the most abundant mineral in the primary oxide ores. The early stage is formed by periodic oxidation of the magma, as a result, for instant of addition of water into the magma. These ore deposits are hosted in serpentinites, ophiolitic metagabbros, amphibolites, metagabbro-tonalite complex, dunite and olivine gabbros.

The metamorphic minerals (chlorite, actinolite and tremolite) and depositional hydrothermal alternation of the oxides (magnetite, ilmenite, titanomagnetite, chromite and magnesioferrite) with the phosphate mineral (apatite), and supergene minerals (kaolinite) actually reflects the stages of mineralization as follows (Table 2). Wadi Zayatit and Wadi Mikbi affected by magmatic activities that represented by granites, basic dykes, and quartz veins. The supergene solutions like meteoric waters, played role especially on the fractured oxides. Supergene alterations could be seen throughout the oxidized zone near the surface, in which moderate and extensive alteration of primary ores occur. Both partial and complete replacements are observed along grain boundaries and internal channel ways such as cleavage and fracture planes (alteration of alkali feldspars into the kaolinite mineral under slightly acidic solutions in supergene conditions) (Table 2).

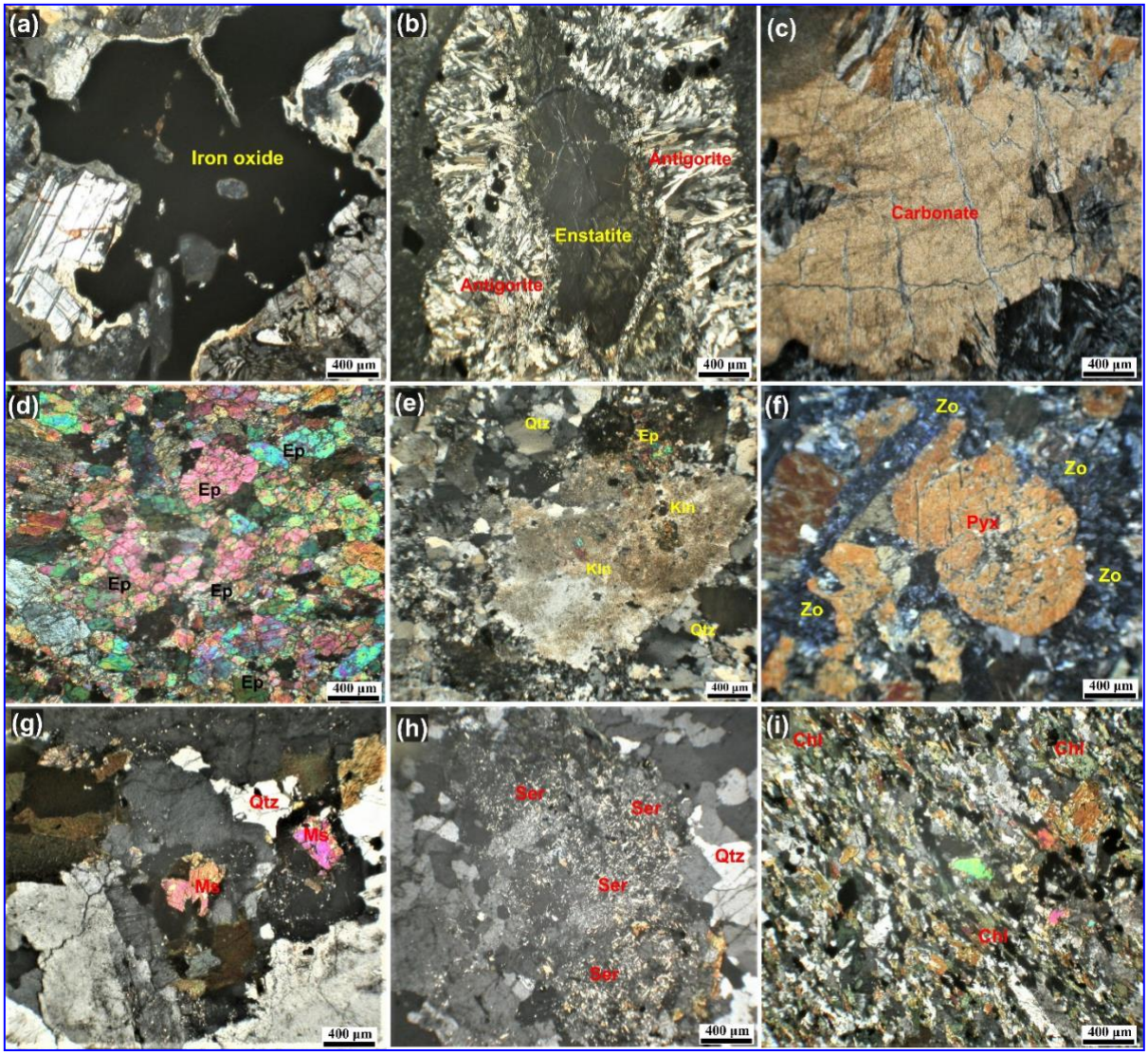

Fig.15. Microphotographs of the altered rock units showing: (a) Oxidization zone found in olivine gabbros. (b) Serpentinization (altered of pyroxene and olivine to enstatite and antigorite) present in serpentinites. (c) Carbonatization crystals present in serpentinites. (d) Epidotization process found in epidosite, which formed from hydrothermally alteration of plagioclase to epidote crystals (Ep). (e) Kaolinitization (Kln) of plagioclase (Pl) crystals and silicification (Qtz) crystals found in the granitic rocks. (f) Zoisitization process formed from alteration of plagioclase to zoisite (Zo) adjacent with the propylitic zone that encountered in the ophiolitic metagabbros. (g) Muscovitization process formed from the alteration of the feldspars to muscovite crystals (Ms) that found in the granitic rocks. (h) Highly alteration of plagioclase (Pl) to sericite (Ser) crystals that encountered in the granitic rocks. (i) Biotite (Bt) flakes partially altered to chlorite (Chl) found in the arc-related metasediments.

4.2.4. Ore microscopy

A detailed study on the genesis of ore and gangue minerals were collected from Wadi Zayatit and Wadi Mikbi rock samples. The specific petrographic features, ore textures, and their opaque minerals of the mineralized rock units show the significant oxide minerals such as magnetite, ilmenite, titanomagnetite, chromite, and magnesioferrite. Magnetite occurs as irregular granular aggregates fine- to coarse-grained, light grey in color with brownish tint. Magnetite is the essential opaque mineral and occurs as subhedral to anhedral crystals (Fig.16a & b). Magnetite crystals recorded in Wadi Zayatit

metagabbros (Fig. 16b) and Wadi Mikbi amphibolites (Figure 16a). Magnetite occurs as homogeneous magnetite and titanomagnetite crystals. It is usually fresh but may be completely altered to martite due to the oxidation of magnetite within the metagabbros and iron-bearing tremolite-actinolite schists at Wadi Zayatit and Wadi Mikbi district. Ilmenite occurs as subhedral elongated crystals of tabular-like shape (Fig. 16c). Usually it occurs as plates, separated grains and as whitish black and grey small bodies.

Table 2. Paragenetic sequence of the mineral deposits in the Wadi Zayatit and Wadi Mikbi rock units.

Mineral deposits	Stages of mineralization			
	Metamorphism stage	Magmatic stage	Hydrothermal stage	Supergene stage
Magnetite				
Titanomagnetite				
Ilmenite				
Chromite				
Magnesioferrite				
Clinochlore				
Chlorite				
Calcite				
Plagioclase				
Sericite				
Epidote				
Zoisite				
Olivine				
Pyroxene				
Hornblende				
Biotite				
Muscovite				
Tremolite				
Actinolite				
Orthoclase				
Quartz				
Antigorite				
Enstatite				
Apatite				
Iddingsite				
Zircon				
Brucite				
Kaolinite				
Tourmaline				
Allanite				
Almandine garnet				

Ilmenite transformed to titanomagnetite that found in Wadi Mikbi olivine gabbros (Fig. 16d), hosted in metagabbro-tonalite complex of Wadi Zayatit and Wadi Mikbi and olivine gabbros of Wadi Mikbi.Titanomagnetite appears as coarse-grained, subhedral to euhedral irregular crystals and exsolution of fine network intergrowth of titanomagnetite in the magnetite and ilmenite crystals exhibit porphyroblastic texture (Fig. 16e & f). Titanomagnetite is formed when magnetite contains lamellar exsolution of ilmenite (Fig.16d). It exhibits grey to light grey color with pinkish tint and moderate reflectance (Figure 16d). In most samples, titanomagnetite occurs as fine anhedral to medium subhedral crystals scattered throughout the whole rock. Titanomagnetite crystals were observed in Wadi Mikbi

olivine gabbros, Wadi Zayatit ophiolitic metagabbros, and Wadi Mikbi iron-bearing amphibolites. Titanomagnetite formed as a result the intergrowth of magnetite and ilmenite crystals within the olivine gabbros and ophiolitic metagabbros at Wadi Zayatit and Wadi Mikbi district. In olivine gabbros and amphibolites, it appears as elongated granules with fine needles of ilmenite forming fine network intergrowth (Fig. 16d & f).

Chromite occurs as isotropic euhedral to subhedral homogenous crystals and zoned crystals of grey color and reddish brown to brown internal reflection, occurs irregular to euhedral fractured crystals with silicate minerals filling the microcracks (Figure 16g). On the other hand, chromites are recorded in Wadi Zayatit serpentinites. Takla (1982) indicated that by increasing serpentinization, the extent of chromite zoning also increases. The inner core of zoned chromite is darker than the outer rim, which is lighter grey in color and has higher reflectivity.

Magnesioferrite occurs as disseminated subhedral grains grey in color and elongated granules crystals (Fig. 16h & i). Magnesioferrite crystals included within Wadi Zayatit serpentinites (Figure 16h) and Wadi Mikbi amphibolites (Fig. 16i).

4.2.4. Mineralogy of the studied mineralized rocks (X-Ray Diffraction)

The studied bulk rock units subjected to crushing, grinding, and grain-size analyses processes. The rock samples are separated into light and heavy fractions by gravity method, treated with water to remove the clay materials, then it is dried for about 10 minutes at more than 200ºC on the oven. The dried fine fractions (0.125 - 0.062mm) are released into a separating funnel. Then, the heavy liquids separation technique by using Bromoform of specific gravity 2.85 gm/cm^3 to concentrate the heavy minerals, which are subjected to X-ray diffraction (XRD) technique. Fifteen samples were separated by gravity method encountered in five rock units viz: serpentinites, ophiolitic metagabbros, amphibolites, dunite, olivine gabbros, and metagabbro-tonalite complex. The identified minerals by XRD technique are magnetite, ilmenite, chromite, titanomagnetite, magnesioferrite, quartz, clinochlore, plagioclase, pyroxene, and epidote (Fig. 17). The X-ray diffraction analyses of the studied rock units confirm the microscopic observation and the SEM/EDX investigations.

4.2.5. Chemistry of some mineral deposits (SEM/EDX)

The EDX analyses identify the elements occur in some analyzed specimens, whereas the quantitative microchemical analyses show how much of a particular element is present in the analyzed specimens. The SEM estimation and the EDX spectra of the thin-polished section from different rock units of the study district could be identify the minerals encountered in these rock units. The studied oxide minerals occurred within the serpentinites, ophiolitic metagabbros, dunite, olivine gabbros, amphibolites, and metagabbro-tonalite complex. EDX microchemical analyses of small thin-polished section of the mineralized rock specimens collected from Wadi Zayatit and Wadi Mikbi reveals the presence of magnetite, ilmenite, titanomagnetite, chromite, magnesioferrite, and apatite.

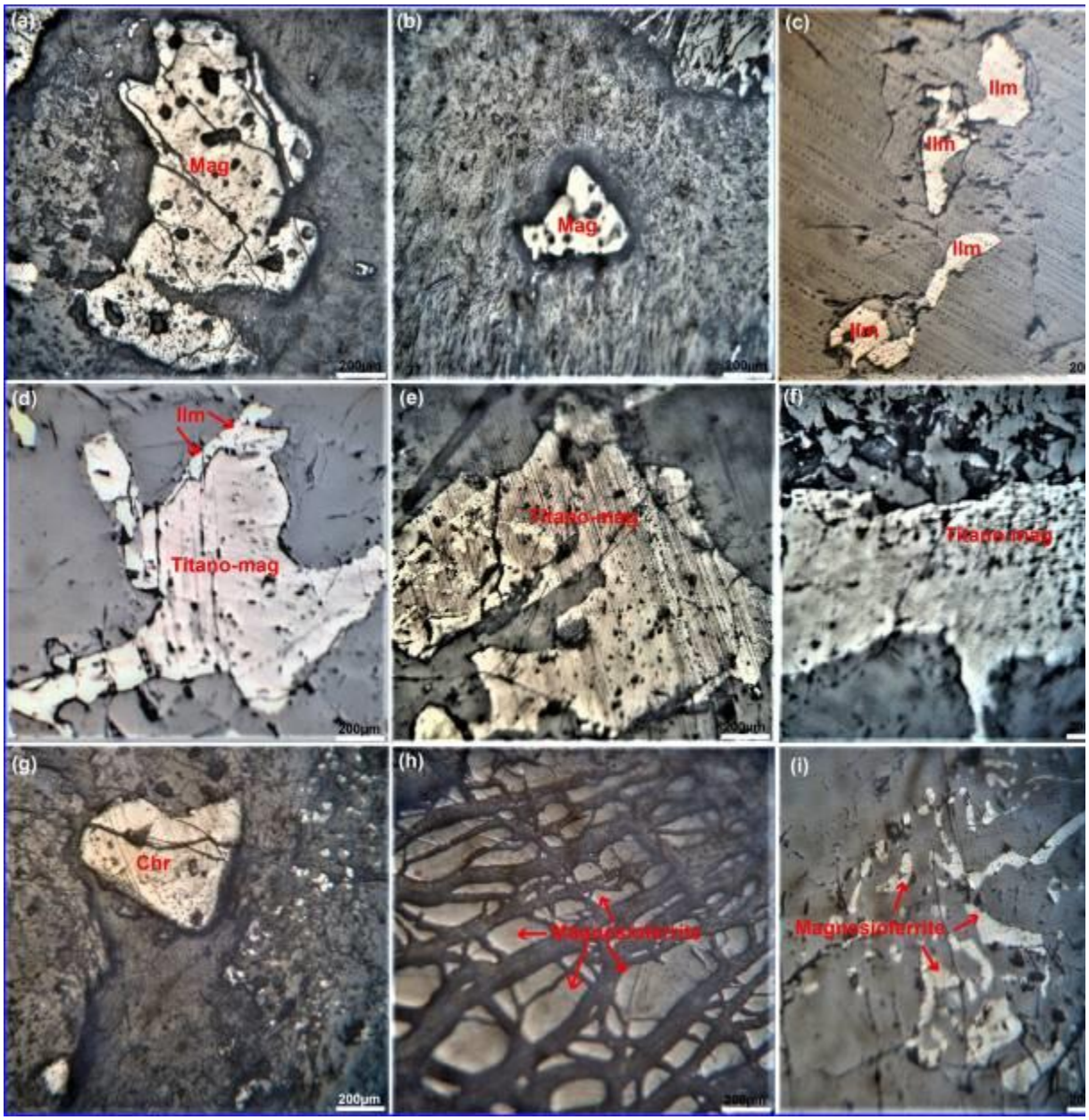

Fig.16. Photomicrographs of the reflected light microscopy. (a) Coarse-grained magnetite crystals (Mg) encountered in the amphibolites. (b) Irregular magnetite crystals (Mg) present in the ophiolitic metagabbros. (c) Subhedral ilmenite crystals (Ilm) found in the metagabbro-tonalite complex. (d) Coarse grains of titanomagnetite (Tit-mag) adjacent with ilmenite crystal present in olivine gabbros (e) Coarse grains of titanomagnetite (Tit-mag) crystals found in the ophiolitic metagabbros. (f) Elongate titanomagnetite (Tit-mag) crystals encountered in the amphibolites. (g) Homogeneous subhedral chromite crystals (Chr) found in the serpentinites. (h) Disseminated anhedral magnesioferrite crystals present in the serpentinites. (i) Anhedral magnesioferrite crystals encountered in the amphibolites.

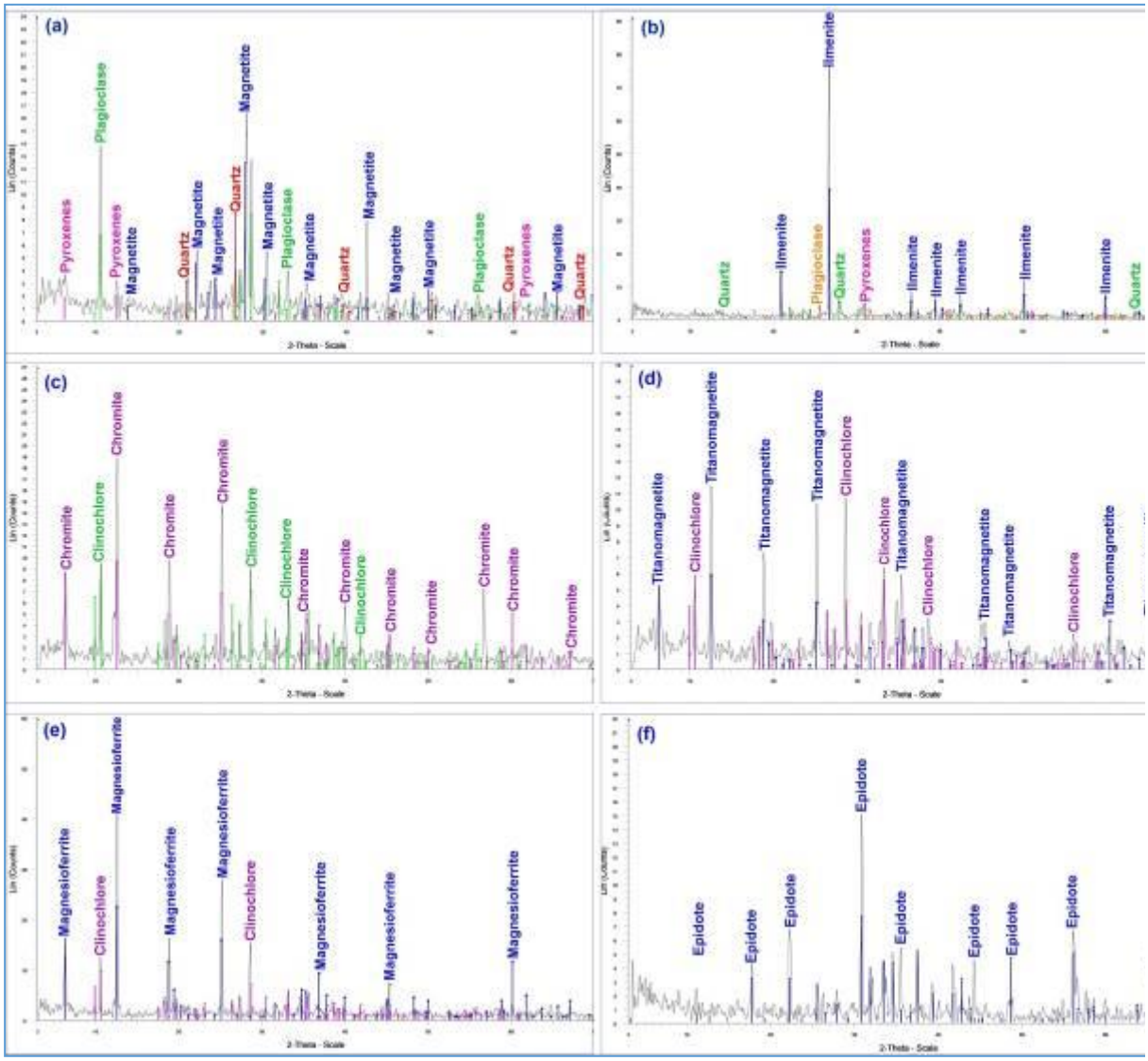

Fig.17. X-ray diffractograms of the heavy fractions of serpentinites, ophiolitic metagabbros, amphibolites, dunite, olivine gabbros, and metagabbro-tonalite complex.

Magnetite, the EDX analyses of coarse-grained magnetite crystals prove to presence of magmatic iron in their obtained elemental composition. EDX microchemical analyses of the magnetite crystals found in the serpentinites (Fig. 18a) and amphibolites (Figure 18b). The X-ray spectrum of magnetite-bearing serpentinites shows high peak of Fe (69.10%). The effect of groundmass enclosing magnetite crystal is reflected by appearance of relatively small peaks of O (16.24%), Cr (4.80%) and Ti (1.74%; Figure 18a). The X-ray spectrum of magnetite–bearing amphibolites shows high peak of Fe (73.29%) and small peaks from O (14.84%), Mg (7.60%), and Si (4.27%; Fig. 18b).

EDX microchemical analyses of fine granular ilmenite crystals are disseminated in metagabbro-tonalite complex (Fig. 18c). The X-ray spectrum of ilmenite-bearing metagabbro-tonalite complex shows high peaks of Ti (43.73%), Ca (28.31%), Si (20.92%), and Fe (4.25%; Fig. 18c).

Titanomagnetite are opaque minerals with compositions between end members magnetite (Fe_3O_4) and ulvöspinel (Fe_2TiO_4). The crystal structure of titanomagnetite is the spinel structure. Disseminated titanomagnetite ores encountered in Wadi Zayatit and Wadi Mikbi intrusion are situated in the amphibolites (Figure 18d), metagabbros (Figure 18e) and olivine gabbros (Figure 18f). EDX microchemical analyses of titanomagnetite displays high peaks of iron (44.91%) and titanium (34.29%; Figure 18d) that recorded amphibolites; high peaks of iron (40.76%) and titanium (36.80%; Fig.18e)

found in the ophiolitic metagabbros, and high peaks of iron (42.74%) and titanium (32.81%; Figure 18f) present in olivine gabbros. Meanwhile the presence of small O, Si, Mn, Mg, and Ca peaks along the spectrum profile of titanomagnetite crystals owing to its contamination of the host rocks.

EDX microchemical analyses of chromite crystals spotted within the ophiolitic metagabbros and dunite (Fig. 19a & b). These analyses display high peaks of Fe (56.73%) and Cr (21.15%) that recorded in the ophiolitic metagabbros (Fig. 19a). The microchemical analysis of chromite crystals found in the dunite displays high peaks of Cr (91.13%) and Fe (2.35%; Fig. 19b). Meanwhile, the presence of small amounts of O, Al, Mg, Ti, Al, Si, and Ca peaks can be attributed to its contamination of the hosted ophiolitic metagabbros and dunite (Fig. 19a & b).

EDX microchemical analyses of magnesioferrite crystals spotted within the amphibolites and serpentinites are shown in Fig.19c & d. These microchemical analyses display high peaks of Si (26.12%), Fe (19.42%), and Mg (17.12%) of the amphibolites (Fig. 19c), the microchemical analysis of magnesioferrite crystals occurred in the serpentinites displays high peaks of Si (28.57%), Fe (27.18%) and O (24.73%; Fig. 19d). Meanwhile, the presence of small amounts of O, Al, Ba, Sr, S, Cu, Ca, K, and Ti peaks can be attributed to its contamination of the hosted ophiolitic metagabbros and dunite (Fig. 19c & d).

EDX microchemical analyses of apatite euhedral grains enclosed within the ophiolitic metagabbros (Fig. 19e). From this figure, the Ca content reaches (54.42%), P (36.8%), and O (16.65%). Furthermore, the presence of Mn (3.26%), Si (1.8%), and Mg (0.73%) peaks of apatite crystals considered to be the contamination of the hosted rocks (Fig 19e).

5. Mineral Potentiality Mapping

All the previous results including the lineament density map and different types of hydrothermal alterations have been cross-linked using an overlay analysis to highlight zones of higher potentiality for mineralization. Weighted overlay analysis was performed in a GIS environment by specifying the same influence for the detected hydrothermal alteration types (Rasters representing ASTER and Sentinel 2 outputs were embedded in that analysis) besides structural density map. The present results revealed that most of the study district has a moderate potentiality. According to the resultant MPM (Figure 20), low potential zones are mainly associated with wadi deposits as a result of the lack of structural features in these low-land districts. Highly potential zones are represented by a limited number of pixels that combine intensive hydrothermal alteration existence and structural dissection. These pixels could be divided into 4 main zones. The first zone represents the extreme northwestern part of the study district where real structural anomalies and hydrothermal alteration products are observed from different remote sensing data (ASTER and Sentinel), and confirmed by using the field observations, and laboratory studies. The second zone is represented by a distributed number of pixels in the central part of the study district. This zone is also confirmed by the laboratory studies and could be gathered with the surrounding moderate potentiality districts to form one of the largest potentially mineralized zones within the study district. The third zone represent a smaller patch at the central southern part of the district. It should be emphasized that the eastern part of the study district constitutes a false mineralized zone where the higher potentiality is given by weathering products and the dissection is mostly by dykes of various compositions.

Detailed inspection of the resultant MPM and their inputs (distribution of hydrothermal alteration and structural density maps) combined with, geological map, field observations, and laboratory studies revealed that oxides constitute the main mineralization type within the study district. According to the mineralogical investigations, the ore minerals include chromites, magnesioferrite, magnetite, magnetite-ilmenite, and titanomagnetite. These ores are mainly confined to dismembered ophiolitic rocks, island arc assemblage, and Alaskan type intrusions. More closely, ophiolitic serpentinite is rich in chromites-

magnesioferrite-magnetite. Magnetite-titanomagnetite-chromites are also recorded with the ophiolitic metagabbros while magnetite-ilmenite is confined to amphibolites. In addition to the previously mentioned ophiolitic sources within the study district, magnetite as one of the most abundant ore types within the study district was also detected with island arc assemblage (Metagabbro-tonalite complex). Additionally, chromites and titanomagnetite were recorded in Alaskan type intrusions represented by dunite and olivine gabbros, respectively. With respect to the MPM, these lithologies are mostly confined to moderate to high potentiality and reasonably coincided with the field investigations and mineralogical examinations.

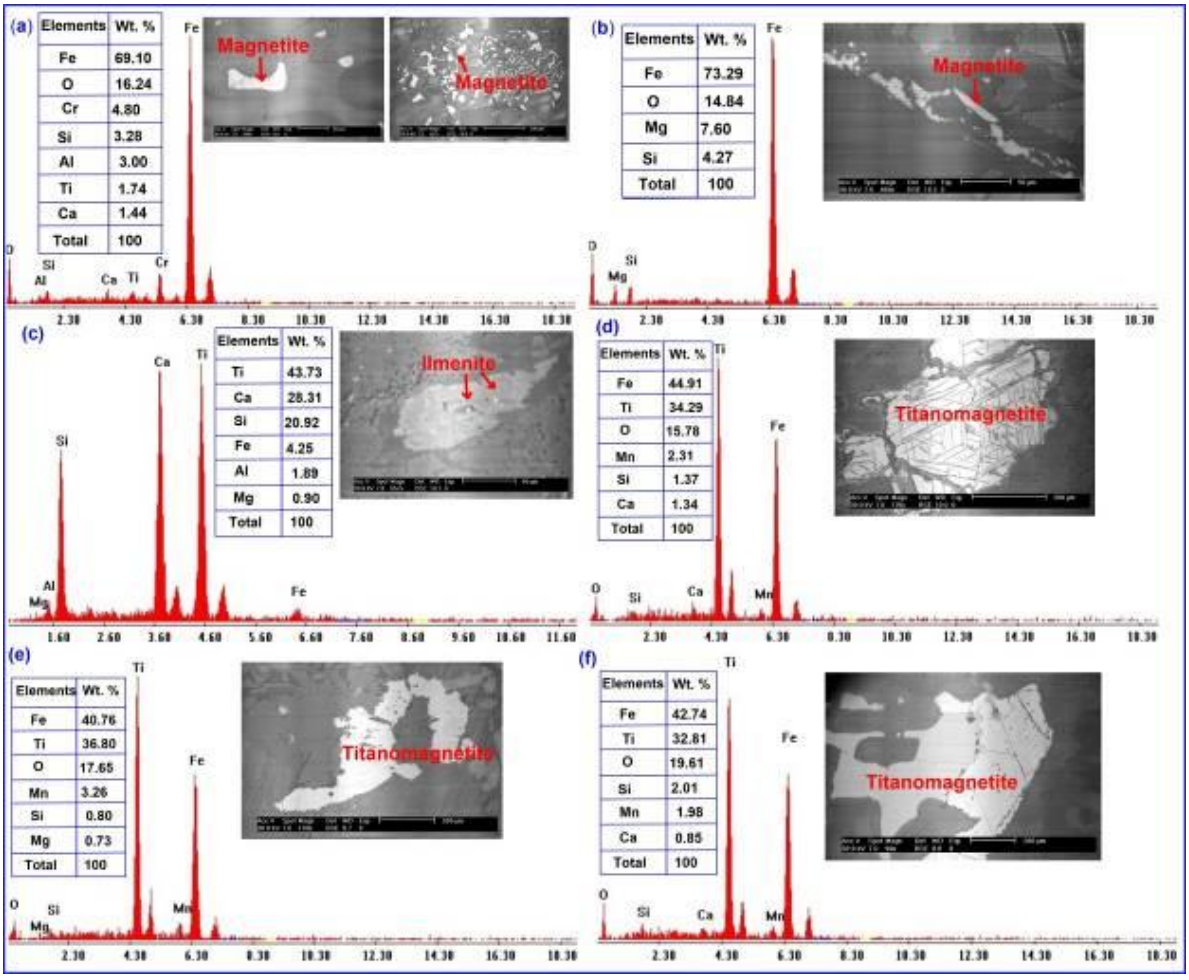

Fig.18. BSE image and EDX spot microchemical analysis showing: (a) Magnetite crystals-bearing serpentinites. (b) Magnetite crystals-bearing amphibolites. (c) Ilmenite crystals-bearing metagabbro-tonalite complex. (d) Titanomagnetite crystals-bearing amphibolites. (e) Titanomagnetite crystals-bearing ophiolitic metagabbros. (f) Titanomagnetite crystals-bearing olivine gabbros.

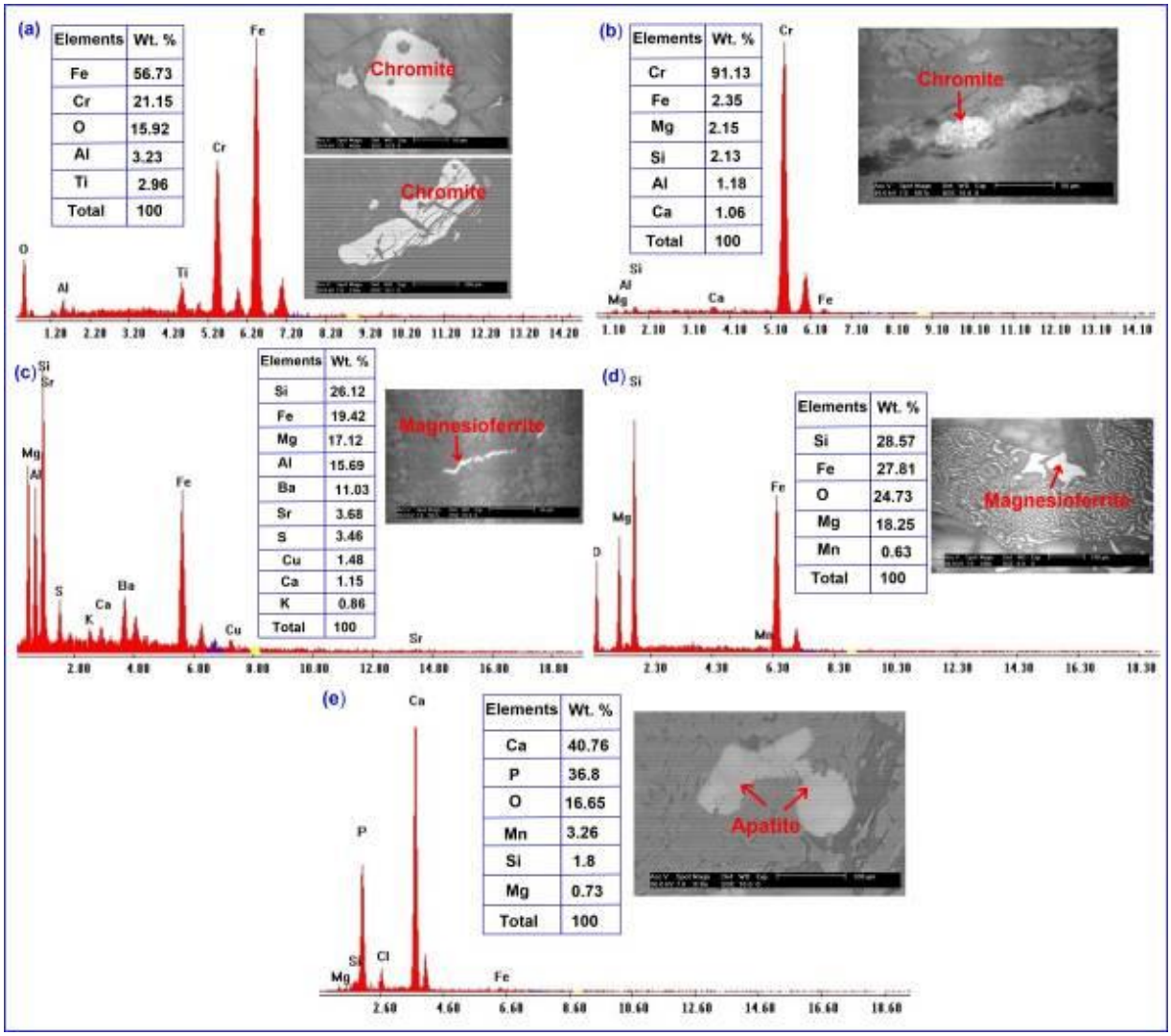

Fig.19. BSE image and EDX spot microchemical analysis showing: (a) Chromite crystals-bearing ophiolitic metagabbros. (b) Chromite crystals-bearing dunite. (c) Magnesioferrite crystals-bearing amphibolites. (d) Magnesioferrite crystals-bearing serpentinites. (e) Apatite crystals-bearing amphibolites.

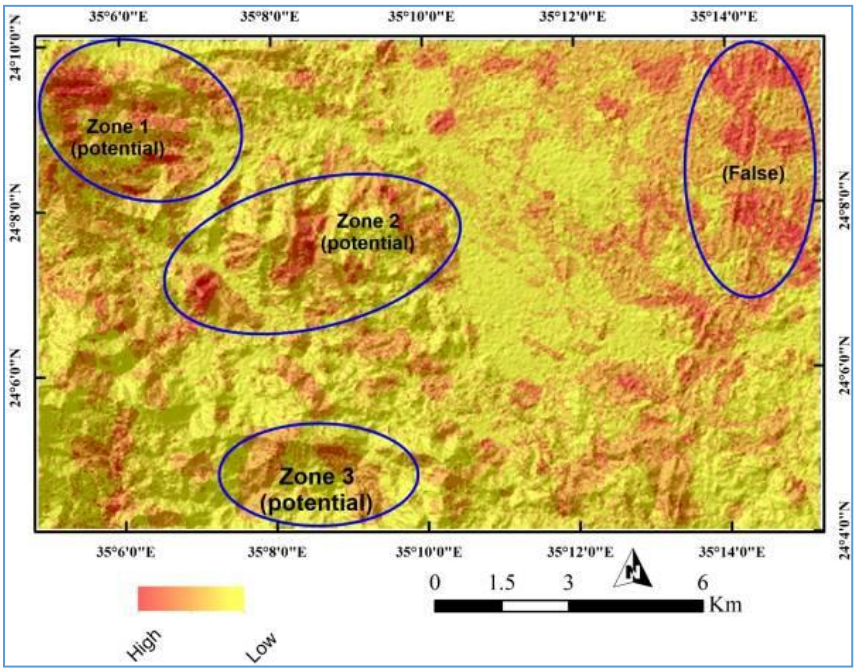

Fig.20. Mineral potentiality map of the study district.

6. Conclusions

The main goal of the current research is to provide an updated lithological map and detect hydrothermal alteration zones to introduce the mineralization potentialities within Wadi Zayatit and Wadi Mikbi district, South Eastern Desert, Egypt. By combining various remote sensing data (ASTER, Sentinel 2, ALOS PALSAR DEM), field observations, petrography of hydrothermal alteration, ore microscopy, X-ray investigations, and EDX analysis, the current study concludes that:

- Reliable lithological allocation could be introduced through Sentinel 2 and ASTER data. Their results are implemented to construct an updated lithological map that is verified with reference to field observations and some previous geological maps.
- Remote sensing data and petrographic examination results confirmed that the dominant hydrothermal alteration minerals within the study district include chlorite, epidote, illite, kaolinite, montmorillonite, muscovite, pyrophyllite, quartz, and calcite.
- The primary types of alteration are oxidization, serpentinization, carbonatization, epidotization, and chloritization. The impacted rocks mainly involve ophiolitic assemblage, island arc rocks and Alaskan-type intrusion. These lithologies encompass significant quantities of iron oxides.
- The main ore deposits in the studied district comprise magnetite, ilmenite, titanomagnetite, chromite, magnesioferrite, and apatite.
- A MPM identifies two main highly potential mineralized zones (magnetite, ilmenite, titanomagnetite, chromite, magnesioferrite, and apatite). Coinciding with the field observations and geological mapping. These zones are hosted primarily by serpentinites, ophiolitic metagabbros, amphibolites, metagabbro-tonalite complex, dunite, and olivine gabbros.
- Integrated remote sensing data, field geology, petrographical studies, and ore mineralogy of the mineral deposits and alteration zones are very helpful in creating a trusted mineral potentiality map of the study region and are strongly recommended as a low-cost reconnaissance exploration program.

Acknowledgements

Ali Shebl is funded by the Stipendium Hungaricum scholarship under the joint executive program between Hungary and Egypt. The authors deeply thank Department Of Geology, Faculty of Science, Al-Azhar University, Department of Mineralogy and Geology, University of Debrecen, and laboratories team of Nuclear Materials Authority (NMA) Egypt, for their help during the practical work.

References

Abd El-Wahed, M., Kamh, S., Ashmawy, M., Shebl, A., 2019. Transpressive structures in the Ghadir Shear Belt, Eastern Desert, Egypt: evidence for partitioning of oblique convergence in the Arabian Nubian Shield during Gondwana Agglutination. Acta Geol. Sin. - English Ed. 93, 1614–1646.

Abdel-Karim, A. A. M., Ali, S., Helmy, H. M., & El-Shafei, S. A., 2016. A fore-arc setting of the Gerf ophiolite, Eastern Desert, Egypt: evidence from mineral chemistry and geochemistry of ultramafic. Lithos, 263, 52-65. DOI.

Abdel-Rahman, A.M., El-Desoky, H.M., Shalaby, B.N.A., Awad, H.A., Antoaneta Ene, Heikal, M.A., El-Awny, H.M., Fahmy, W.M., Taalab, S.A., Zakaly, H.M.H., 2022. Ultramafic Rocks and Their Alteration Products from Northwestern Allaqi Province, Southeastern Desert, Egypt: Petrology, Mineralogy, and Geochemistry.

Abdelkader, M.A., Watanabe, Y., Shebl, A., El-Dokouny, H.A., Dawoud, M., Csámer, Á., 2022. Effective delineation of rare metal-bearing granites from remote sensing data using machine learning methods: A case study from the Umm Naggat Area, Central Eastern Desert, Egypt. Ore Geol. Rev. 150, 105184.

Aboelkhair, H., Ibraheem, M., El-Magd, I.A., 2021. Integration of airborne geophysical and ASTER remotely sensed data for delineation and mapping the potential mineralization zones in Hamash district, South Eastern Desert, Egypt. Arabian. Journal Geoscience, 14, 1–22.

Abu El-Russ, M.A., 1991. Geological Studied on the Abu Ghalaga Area, South Eastern Desert Egypt. M.Sc. Thesis, Faculty of Science, Assiut University, 255.

Ali K., Azer M., Gahlan, H., Wilde, S., Samuel, M., Stern, R. J., 2010. Age of formation and emplacement of Neoproterozoic ophiolites and related rocks along the Allaqi Suture, south Eastern Desert, Egypt. Gond. Res. 18, 583–595.

Badawi, M., Abdelatif, M., Shebl, A., Makroum, F., Shalaby, A., Nemeth, N., 2022. Mapping structurally controlled alterations sparked by hydrothermal activity in the Fatira-Abu Zawal Area, Eastern Desert, Egypt. Acta Geol. Sin. - English Ed.

Basta, E.Z., Kamel, M., 1970. Mineralogy and ceramic properties of some Egyptian talcs. Faculty of Science, Cairo University, Egypt, 43, 285-299.

Basta, E.Z., Takla, M.A., 1968. Petrological Studies on Abu Ghalaga Ilmenite Occurrence, Eastern Desert, Egypt, Geol., 12, 43-71.

Cardoso-Fernandes, J., Teodoro, A.C., Lima, A., Roda-Robles, E., 2020. Semi-Automatization of Support Vector Machines to Map Lithium (Li) Bearing Pegmatites. Remote Sensing, 12, 2319.

Drusch, M., Del Bello, U., Carlier, S., Colin, O., Fernandez, V., Gascon, F., Hoersch, B., Isola, C., Laberinti, P., Martimort, P., 2012. Sentinel-2: ESA's optical high-resolution mission for GMES operational services. Remote Sensing Environment,120, 25–36.

EGSMA., 1988. Ores in Egypt, Information Package/ Prepared by EGSMA with the cooperation of Shell Winning N.V / Cairo 1988.

EGSMA., 1997. Geological Survey of Egypt, Geological map of Egypt, Scale 1:250,000, NG 36 D Sheet.

El-Bahariya GA., 2019. Geochemistry and tectonic setting of Neoproterozoic rocks from the Arabian-Nubian Shield: Emphasis on the Eastern Desert of Egypt. IntechOpen, Geochemistry and Tectonic Setting of Neoproterozoic Rocks from the Arabian-Nubian Shield.

El-Bahariya, G. A., 2021. Ghadir Ophiolites, Eastern Desert, Egypt: A Complete Sequence of Oceanic Crust in the Arabian-Nubian Shield. In the Geology of the Arabian-Nubian Shield, 331-342.

El-Desoky, H.M., Abdel-Rahman, A.M., Antoaneta Ene, Khalil, A.E., Fahmy, M.W., Zakaly, H.M.H., Awad, H.A., 2022b. Origin and Heavy Metals of Plagio-Granites in Egyptian Shield Oceanic Complexes: A Case Study of Abu Dabbab Area, Central Eastern Desert, Egypt. Minerals, 12, 109.

El-Desoky, H.M., Soliman, N., Heikal, M.A., Abdel-Rahman, A.M., 2021. Mapping hydrothermal alteration zones using ASTER images in the Arabian–Nubian Shield: A case study of the northwestern Allaqi District, South Eastern Desert, Egypt. Journal of Asian Earth Sciences: X 5, 100060.

El-Desoky, H.M., Tende, A.W., Abdel-Rahman, A.M., Antoaneta Ene, Awad, H.A., Fahmy, M.W., El-Awny, H.M., Zakaly, H.M.H., 2022a. Hydrothermal Alteration Mapping Using Landsat 8 and ASTER Data and Geochemical Characteristics of Precambrian Rocks in the Egyptian Shield: A Case Study from Abu Ghalaga, Southeastern Desert, Egypt. Remote Sensing, 14, 3456.

El-Magd, I.A., Mohy, H., Basta, F., 2015. Application of remote sensing for gold exploration in the Fawakhir area, Central Eastern Desert of Egypt. Arabian Journal Geoscience, 8, 3523–3536.

Emam, A., Zoheir, B., Johnson, P., 2016. ASTER-based mapping of ophiolitic rocks: Examples from the Allaqi-Heiani suture, SE Egypt. Int. Geol. Rev. 58, 525–539.

Ford, J.H. and Green, D.C., 1977. An oxygen- and hydrogen-isotope study of the Panguna porphyry-copper deposit, Bougainville. Australian Journal Earth Science, 24 (1), 63-80.

Hamimi, Z., Hagag, W., Fritz, H., Baggazi, H., Kamh, S., Hamimi, Z., Hagag, W., Fritz, H., Baggazi, H., Kamh, S., 2022. The Tectonic Map and Structural Provinces of the Late Neoproterozoic Egyptian Nubian Shield: Implications for Crustal Growth of the Arabian–Nubian Shield (East African Orogen). FrEaS 10, 921521.

Hamimi, Z., Hagag, W., Kamh, S., El-Araby, A., 2020. Application of remote-sensing techniques in geological and structural mapping of Atalla Shear Zone and Environs, Central Eastern Desert, Egypt. Arabian Journal Geoscience, 13.

Harlov, D.E., Austrheim, H., 2013. Metasomatism and the Chemical Transformation of Rock: The Role of Fluids in Terrestrial and Extraterrestrial Processes. Springer, 789.

Hu, B., Xu, Y., Wan, B., Wu, X., Yi, G., 2018. Hydrothermally altered mineral mapping using synthetic application of Sentinel-2A MSI, ASTER and Hyperion data in the Duolong area, Tibetan Plateau, China. Ore Geology Review, 101, 384–397.

Hunt, G.R., 1977. Spectral signatures of particulate minerals in the visible and near infrared. Geophysics, 42, 501–513.

Hunt, G.R., Ashley, R.P., 1979. Spectra of altered rocks in the visible and near infrared. Economic Geology, 74, 1613–1629.

Ibrahim, E., Barnabé, P., Ramanaidou, E., Pirard, E., 2018. Mapping mineral chemistry of a lateritic outcrop in New Caledonia through generalized regression using Sentinel-2 and field reflectance spectra. International Journal Applied Earth, 73, 653–665.

Kotb, H., Khaffagy, M.B., Swifi, B.M., 1980. Geochemistry and petrochemistry of Egyptian titaniferous gabbros. Egypt, 627 – 650.

Liu, L., Zhou, J., Jiang, D., Zhuang, D., Mansaray, L.R., Zhang, B., 2013. Targeting mineral resources with remote sensing and field data in the Xiemisitai Area, West Junggar, Xinjiang, China. Remote Sensing, 5, 3156-3171 5, 3156–3171.

Loizenbauer, J., Wallbrecher, E., Fritz, H., Neumayr, P., Khudeir, A. A., & Kloetzli, U., 2001. Structural geology, single zircon ages and fluid inclusion studies of the Meatiq metamorphic core complex: implications for Neoproterozoic tectonics in the Eastern Desert of Egypt. Precambrian Research, 110(1-4), 357-383.

Madbouly, M.I., 2000. Comparative study on petrology and geochemistry of some mafic-ultramafic intrusion of the South Eastern Desert and Sinai, Egypt. Faculty Science, Cairo Univ., Egypt, 200.

Mars, J.C., Rowan, L.C., 2010. Spectral assessment of new ASTER SWIR surface reflectance data products for spectroscopic mapping of rocks and minerals. Remote Sensing Environment, 114, 2011–2025.

Maurice, A. E., Bakhit, B. R., Basta, F. F., & Khiamy, A. A., 2013. Geochemistry of gabbro and granitoids (M- and I-types) from the Nubian Shield of Egypt: Roots of Neoproterozoic intra-oceanic island arc. Precambrian Research, 224, 397-411.

Mielke, C., Boesche, N.K., Rogass, C., Kaufmann, H., Gauert, C., de Wit, M., 2014. Spaceborne mine waste mineralogy monitoring in South Africa, applications for modern push-broom missions: Hyperion/OLI and EnMAP/Sentinel-2. Remote Sensing, 6, 6790-6816 6, 6790–6816.

Munha, J., Fyfe, W.S., and Kerrich, R., 1980. Adularia, the characteristic mineral of felsic spilites. Contributions to Mineralogy and Petrology, 75, 15-19.

Noori, L., Pour, A., Askari, G., Taghipour, N., Pradhan, B., Lee, C.-W., Honarmand, M., 2019. Comparison of different algorithms to map hydrothermal alteration zones using ASTER remote sensing data for polymetallic vein-type ore exploration: Toroud–Chahshirin Magmatic Belt (TCMB), North Iran. Remote Sens. 11, 495.

Pirajno, F., 2009. Hydrothermal processes and mineral systems. Geological Survey of Western Australia. P104-120.

Pour, A.B., Hashim, M., 2012. The application of ASTER remote sensing data to porphyry copper and epithermal gold deposits. Ore Geology Review, 44, 1–9.

Ramadan, A. M., Farghaly, M., Fathy, W. M., & Ahmed, M. M., 2016. Leaching and kinetics studies on processing of Abu-Ghalaga ilmenite ore. International Researcher Journal Engineering Technical, 3, 46-53.

Ries, A, Shackelton R, Graham R, Fitches W., 1983. Pan-African structures, ophiolites and mélange in the Eastem Desert of Egypt: a traverse at 26°N.

Sabins, F.F., 1997. Remote Sensing: Principles and Interpretation, 494pp. New Yark WH Free. Co.

Salem, S.M., 2017. Field Hyperspectral Spectrometer measurements for exploring new Ilmenite and iron oxide occurrences at Abu Ghalaga area, Southern Eastern Desert, Egypt, Vol-6, Numero/17. Gis& Geospace Applications.

Salem., 2018. Ilmenite exploration at Abu Ghalaga area, South Eastern Desert, Egypt, using remote sensing and field Hyperspectral measurements.

Sekandari, M., Masoumi, I., Pour, A.B., Muslim, A.M., Rahmani, O., Hashim, M., Zoheir, B., Pradhan, B., Misra, A., Aminpour, S.M., 2020. Application of Landsat-8, Sentinel-2, ASTER and WorldView-3 Spectral Imagery for Exploration of Carbonate-Hosted Pb-Zn Deposits in the Central Iranian Terrane (CIT). Remote Sensing,12, 1239 12, 1239.

Shackleton RM, Ries RM, Graham RH, Fitches WH., 1980. Late Precambrian ophiolitic mélange in the Eastern Desert of Egypt. Nature (London) 285:472–474.

Shebl, A., Abdellatif, M., Elkhateeb, S.O., Csámer, Á., 2021a. Multisource data analysis for gold potentiality mapping of Atalla Area and its environments, Central Eastern Desert, Egypt. Minerals,11, 641 11, 641.

Shebl, A., Abdellatif, M., Hissen, M., Ibrahim Abdelaziz, M., Csámer, Á., 2021b. Lithological mapping enhancement by integrating Sentinel 2 and gamma-ray data utilizing support vector machine: A case study from Egypt. International Journal Applied Earth, 105, 102619.

Shebl, A., Csámer, Á., 2021a. Lithological, structural and hydrothermal alteration mapping utilizing remote sensing datasets: a case study around Um Salim area, Egypt. IOP Conf. Ser. Earth Environment Science 942, 012032.

Shebl, A., Csámer, Á., 2021b. Stacked vector multi-source lithologic classification utilizing Machine Learning Algorithms: Data potentiality and dimensionality monitoring. Remote Sensing. Applied Society Environment, 100643.

Shebl, A., Csámer, Á., 2021c. Reappraisal of DEMs, Radar and optical datasets in lineaments extraction with emphasis on the spatial context. Remote Sens. Applied Society Environment, 24, 100617.

Shebl, A., Kusky, T., Csámer, Á., 2022. Advanced land imager superiority in lithological classification utilizing machine learning algorithms. Arabian Journal Geoscience, 159 (15), 1–13.

Soliman, N., El-Desoky, H.M., Heikal, M.A., Abdel-Rahman, A.M., 2021. Using ASTER images and field work data for geological mapping around Wadi Umm Ashira and Wadi Tilal Al-Qulieb, Northwestern part of Wadi Allaqi, South Eastern Desert, Egypt. Arabian Journal of Geosciences, 14, 1826.

Stern, R.J., 1994. Arc assembly and continental collision in the Neoproterozoic east African Orogen: implications for the consolidation of Gondwanaland. Annual Review, Earth Planet Science, 22, 319–351.

Stern, R.J., Johnson, P.R., Kröner, A. and Yibas, B., 2004. Neoproterozoic ophiolites of the Arabian-Nubian shield. Developments in Precambrian Geology, 13, 95-128.

Takla, M.A., 1982. Chromites from the Bergen Arcs ultramafics. Neues Jahrbuch für Mineralogie-Abhandlungen, 56-72.

Van der Meer, F.D., van der Werff, H.M.A., van Ruitenbeek, F.J.A., 2014. Potential of ESA's Sentinel-2 for geological applications. Remote Sensing Environment. 148, 124–133.

Walshe, J.L., 1986. A six-component chlorite solid solution model and the conditions of chlorite formation in hydrothermal and geothermal systems. Economic Geology, 81(3), 681-703.